Journal of Fluids and Structures 26 (2010) 918–953

JOURNAL OF
FLUIDS AND
STRUCTURES

www.elsevier.com/locate/jfs

Some aspects of the flip-through phenomenon: A numerical study based on the desingularized technique

Y.-M. Scolan

Ecole Centrale Marseille, Institut de Recherche sur les Phénomènes Hors Equilibre, 13451 Marseille cedex 20, France

Received 20 November 2009; accepted 19 May 2010
Available online 26 June 2010

Abstract

Flip-through is known as a rapidly focusing phenomenon at a wall leading to high loads without impact of liquid. In order to simulate numerically these highly nonlinear waves, the boundary value problem is formulated in potential theory without surface tension. A desingularized technique is used to compute the velocity potential. Conformal mappings of the fluid domain simplify the formulation of the solution.

As shown by many contributors to the method of fundamental equations (another name to denote desingularized methods), the suitable desingularizing distance must be chosen with care. Here the criteria for choosing it follow from energy and mass conservation laws. This study shows what is the influence of an arbitrary additive constant to the velocity potential regarding conservation laws. Validation tests are performed on a focused wave. Recommendations are given regarding the choice of the desingularizing distance and the additive constant as well.

In order to better control the initiation of flip-through, the simulations start from an initial free surface deformation in a rectangular tank, with or without varying bathymetry. The subsequent jet running along the wall, is described and the corresponding loads are discussed. In particular in the present configuration, it is shown that, along the wall, the maximum acceleration precedes the maximum of pressure contrary to the findings of previous studies. The sensitivity of the results with regard to the shape of the initial deformation and the local bathymetry is discussed.

Keywords: Desingularized method; Flip-through

1. Introduction

Among the numerous numerical methods for solving two-dimensional nonlinear free surface equations in potential theory, there are some techniques which appear to be the simplest in terms of computational needs. In the footsteps of Tuck (1998), we implement one of them in order to achieve highly deformed free surfaces with minimum computational effort. To this end a desingularized technique is coupled to a conformal mapping scheme. The former method provides a convenient framework for solving the potential flow problem. The latter technique substantially simplifies the equations to be solved.

E-mail address: ymscolan@centrale-marseille.fr

doi:10.1016/j.jfluidstructs.2010.06.002

Desingularized techniques belong to the so-called Methods of Fundamental Solutions. A special issue of *Engineering Analysis with Boundary Elements* (Volume 33, Issue 12, 2009) recalls the main steps from the pioneering work by Kupradze and Aleksidze (1963) up to the numerous applications either for the rolling up of vortex sheet as done in Krasny (1986), or the wave motion as done in Cao et al. (1991) among others.

In the present paper we are concerned with highly nonlinear free surface motion and the considered flows are two-dimensional. The general framework follows from the equivalence between the flow kinematics around an obstacle (inner or outer problem) and a distribution of singularities. The type of singularity depends on the type of operator and possibly on the type of boundary conditions. Here the flow is described by the Laplace equation, hence the corresponding Green function is the Rankine source. As we consider two-dimensional flows, this Rankine source potential is a simple *Log* function. The principle of the desingularized method is to place the singularities (defined by the Green function) at a short distance from the actual interface. In the present application, the singularities are only distributed close to the actual free surface. There is a clear difference between two-dimensional and three-dimensional applications since for the former case, complex variable theory applies while for the latter case, numerical implementation, at least in terms of panelling the fluid boundaries, requires as much effort as for any other classical boundary element method, equations are derived in Webster (1975) or Gao and Zou (2008).

When using the desingularized method, we face the difficulty of the arbitrary choice of the short distance at which the singularities are located. Alves (2009) gives some theoretical criteria and underlines the balance between accuracy and ill-conditioning depending on the distance between the source points and the actual support of the boundary condition. Young et al. (2005) assess the accuracy by applying the technique to the flow around a circle with zero circulation for which an exact solution exists. For applications regarding the wave motion, this point is highlighted by Cao et al. (1991). In their approach the singular points are located in the normal direction of the interface at a distance

$$\frac{L_d}{L} = \ell_d \sqrt{\frac{D_m}{L}}, \tag{1}$$

where L is a length scale, ℓ_d controls the amplitude of the desingularization. The parameter D_m is a measure of the discretization, that is to say the distance between two consecutive markers. In their rather academic numerical tests, Cao et al. (1991) show that there exists a minimum value of ℓ_d for which the accuracy is the best. Zhang et al. (2006) simulate a soliton riding over a submerged bar and they adapt ℓ_d to those applications. By studying sloshing in a rectangular tank, Tuck (1998) distinguishes the weakly nonlinear case from the highly nonlinear case. For the former case he proposes placing each singularity along a vertical line originating from the associated marker which belongs to the free surface. For strongly distorted free surfaces, the sources are placed along the normal to the free surface from the associated marker. He proposed the distance

$$L_d = \alpha \frac{L}{N}, \quad 2 \le \alpha \le 3, \tag{2}$$

where L is the length of the tank and N is the number of markers. Tuck further underlines that his computations do not require any smoothing.

It is not the purpose of the present paper to numerically analyze either the convergence or the ill-conditioning of the problem in terms of the desingularizing parameter L_d. We rather proceed heuristically by tuning the parameter L_d up to a value for which most applications work. The main reason for that is we consider highly nonlinear waves for which we do not have any exact solutions. The only checking that can be done is the conservation of mass and energy. The problem of conservation of mass and energy for unsteady flows is barely described in the literature when desingularized techniques are used. Yet these are important features and we observe here that invariants (mass and energy) are mainly conserved in time. However, when studying flip-through phenomena, an artificial increase of kinetic energy may occur. This study aims to quantify these discrepancies. Recommendations are given to keep these discrepancies to a minimum.

It is also the purpose of the present work to numerically examine the flip-through phenomenon. Since the pioneering work by Cooker and Peregrine (1990), few numerical studies have been done on this topic. Longuet-Higgins and Oguz (2005, 2007) and Longuet-Higgins (2001), starting from plausible free surface profiles and distribution of potential, arrived at the expected jets with high accelerations. Recently Cooker (2010) investigated possible solutions of the nonlinear free surface boundary conditions. He shows that the change of concavity of the free surface corresponds to the occurrence of a pressure peak then an acceleration peak. In the present numerical study we shall show that this chronology is inverted. The simplest explanation is that Cooker (2010) deals with a local solution without accounting for the influence of the rest of the flow. We should gain further insights into this difference by performing a very localized parametric study on the basis of the technique detailed in Section 3.4.

It is difficult to perform experimental analysis of the flip-through phenomenon. The reasons are twofold: (i) we need not only a high resolution in space but also a very high resolution in time; (ii) the control and repeatability of the flow is a difficult task and requires much care. Typical features of the phenomenon are the occurrence of both a pressure peak and an acceleration peak. Even if a high speed camera may provide the fluid motion, derivatives are required to get the full kinematics including acceleration. Uncertainties are also well known while measuring the pressure peak. In spite of repeated experiments, dispersion around mean values cannot be avoided. Yet some experimental studies exist. Lugni et al. (2005, 2006) proposed a classification of flip-through into three types, depending mainly on the wave profile before impact. However, flip-through, as described by Cooker and Peregrine (1990), can be considered as the transition between the fully developed cavity which collapses and a simple run-up along the wall. A precise description of the phenomenon is urgently required in order to better understand the physical mechanisms of this transition.

It is the purpose of this paper to describe some recent results obtained with the technique outlined above. The following developments start with a description of the numerical schemes: desingularized method and conformal mapping (Sections 2.1–2.4). The different initial conditions studied are listed in Section 2.5 and conservation laws are established in Section 2.6. The combined influences of the desingularizing distance and the additive constant to the velocity potential are analyzed in Sections 2.7 and 2.8. Applications are presented in Section 3. In particular, it is shown that the occurrence of the flip-through phenomenon is highly dependent on the variation of the parameters defining the initial conditions (see Section 3.1). However, when it occurs, its evolution is independent of the type of the initial conditions used to generate it (see Section 3.3). Perspectives for future work are outlined in Sections 3.4 and 3.5 regarding the influence of a local bathymetry and some artificial techniques which allow a wider parametric study.

2. Numerical modelling

The fluid domain is denoted $\Omega(t)$, its boundary is denoted $\partial\Omega(t)$ and the free surface $Fs(t)$ is a part of it. That is illustrated in Fig. 1.

The governing partial differential equation is the Laplace equation for the velocity potential. We prescribe homogeneous Neumann boundary conditions on walls since they are impermeable and they do not move in time. On the free surface we classically prescribe the continuity of stress and velocity.

The implemented numerical scheme is composed of two techniques. In a first step, different conformal transformations are sequentially implemented, so that the solid boundaries of the fluid domain are turned into a rectilinear axis. By mirroring the free surface line with respect to this rectilinear axis, the fluid domain is closed. That is the key feature of the present model since the resulting boundary value problem is an interior Dirichlet problem and Dirichlet boundary conditions are only prescribed on the free surface. The velocity potential is hence broken down into elementary solutions which implicitly account for the homogeneous Neumann boundary conditions on the impermeable solid walls. This BVP reads

$$\Delta\phi = 0 \text{ in the fluid}, \quad \phi = e(\vec{M},t) \text{ on the free surface}, \tag{3}$$

where $\vec{M}$ denotes the two-dimensional position of point M on the free surface and the function e follows from the solution of the time differential system composed of kinematic and dynamic free surface boundary conditions.

This section describes how the conformal mappings are built and how to solve BVP (3).

2.1. Conformal mapping

When solving the two-dimensional Laplace equation through the use of a Green function, it is worthwhile searching for a coordinate system in which the boundary conditions can be implicitly accounted for in the expression of the Green function. That depends on the simplicity of the geometry. Conformal mappings are hence used to obtain the new suitable coordinate system.

Conformal mapping is not used to map the instantaneous fluid domain, but only the domain bounded by the walls of the tank whatever its filling ratio. For a simple rectangular tank with flat bottom, the physical domain

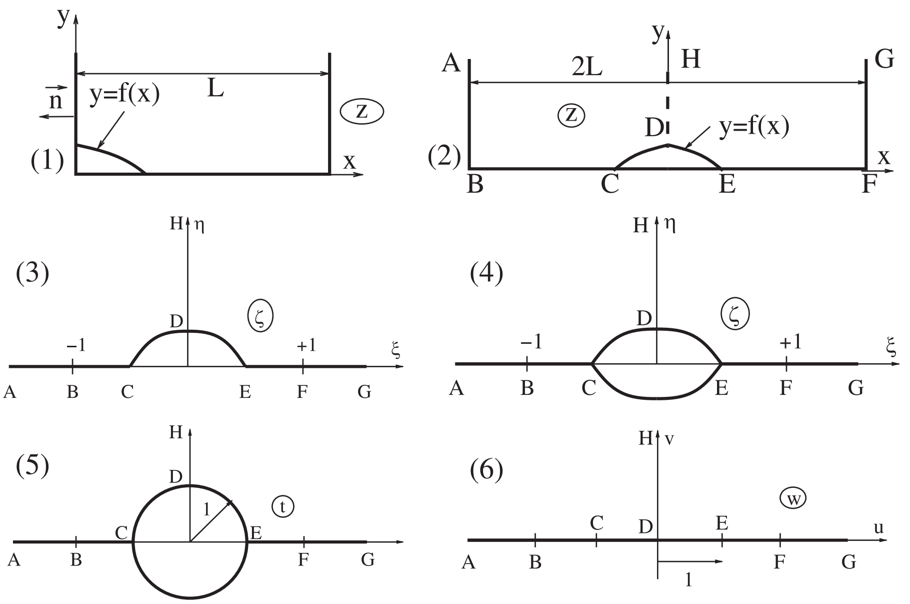

Fig. 1. Successive conformal transformations used to account for a bathymetry. (1) original physical plane, the length of the tank is L. The nonhorizontal bathymetry is defined by the equation $y=f(x)$ in the coordinate system $(0,\vec{x},\vec{y})$ centered at the lower left corner. In this plane the fluid domain is denoted $\Omega(t)$, with boundary $\partial\Omega(t)$ and the free surface $FS(t)$ is a part of it. (2) addition of the symmetrical domain with respect to the vertical axis $x=0$, due to symmetry the segment DH is no longer a material boundary, (3) domain after Schwartz–Christoffel transformation defined by Eq. (5), (4) addition of the symmetrical domain with respect to the horizontal axis $\eta=0$, (5) domain after Karman–Trefftz (corner removal procedure at points C, D and E) and Theodorsen–Garrick transformations which turns a near circle into a unit circle, (6) domain after transformation (8).

is hence a semi-infinite strip. When there is a bathymetry along the bottom, in addition, a sequence of standard conformal transformations are used to tackle simply connected bodies; details can be found in Scolan and Etienne (2008).

In the present case we basically consider a rectangular basin with length L. The fluid is then contained in a semi-infinite strip defined in the physical coordinate system as illustrated in Fig. 1(1). The origin O of the coordinate system is always located at the bottom left corner. The horizontal and vertical axes are denoted x and y, respectively, with the corresponding normalized vectors $\vec{x}$ and $\vec{y}$. A bathymetry can be introduced in the tank; it is defined by the equation $y=f(x)$.

If the bottom is flat and horizontal, we use Schwartz–Christoffel transformation, that is described in Spiegel (1999, p. 206) with a sign error

$$\zeta=-\cos\frac{\pi z}{L}. \tag{4}$$

Then the images of the vertical walls are now located along the real axis of $\zeta-$plane. If there is a bathymetry, we use Schwartz–Christoffel transformation

$$\zeta=\sin\frac{\pi z}{2L}, \tag{5}$$

and from the Z-plane (see Fig. 1(1)), including its symmetric part with respect to the left vertical wall (Z-plane in Fig. 1(2)), we get the $\zeta-$plane (see Fig. 1(3)), by “flattening” the two end walls placed at $x=\pm L$. Then the symmetric domain with respect to the horizontal axis is introduced (see Fig. 1(4)). The local bathymetry and its images is now a closed contour. There are corners along this contour. Those corners exist if $\mathrm{d}f/\mathrm{d}x\neq O$ at point D, if $|\mathrm{d}f/\mathrm{d}x|\neq\infty$ at points C or E or at any point when $\mathrm{d}f/\mathrm{d}x$ is not continuous. In order to further transform the domain into a simpler one, we use the Karman–Trefftz (KT) transformation as described in Halsey (1979). The formula of this transformation links the new complex coordinate ζ' to the original complex coordinate ζ, and it reads

$$\zeta' = \frac{1}{2}\frac{Z_t - Z_c}{(2-\alpha/\pi)}\frac{1+\left(\dfrac{\zeta - Z_t}{\zeta - Z_c}\right)^{1/(2-\alpha/\pi)}}{1-\left(\dfrac{\zeta - Z_t}{\zeta - Z_c}\right)^{1/(2-\alpha/\pi)}}, \tag{6}$$

where α is the inner angle at a given corner and the complex coordinate $\zeta = Z_c$ denotes a geometrical center of the shape. The transformation 6 turns a shape with corner at complex coordinates $\zeta = Z_t$ into a shape which is smooth at the image ζ' of $\zeta = Z_t$. The transformation 6 is used as much as necessary for each corner along the contour. However due to double symmetry of the shape, this operation can be optimized. After removing all the corners, the obtained shape is smooth but it does not have a regular contour. A Theodorsen–Garrick (TG) transformation as described in Theodorsen and Garrick (1933), is then used. The corresponding conformal function links the original complex coordinate ζ' to the new complex coordinate t, it reads

$$\zeta' = t \cdot \exp^{\left[\sum_{n=0}^{\infty} \beta_n t^{-n}\right]}. \tag{7}$$

The complex coefficients β_n are computed via a fixed point scheme and Fast Fourier Transform as described in Ives (1976). In practice an accuracy of 10^{-12} is imposed. At convergence, a perfect circle is obtained. It is worth recalling that Warchawski (1945) provides conditions on the speed of the iterative scheme: the closer to a circle the shape in ζ'−plane, the faster the fixed point algorithm. The combination of KT transformation and TG transformation is illustrated by passing from sketch (1–4) to (1–5) in Fig. 1.

Finally we arrive at a unit circle in the t-plane. We use the transformation

$$w = \frac{1}{2}\left(t + \frac{1}{t}\right), \tag{8}$$

which turns the outer domain of the unit circle into the outer domain of a flat plate lying on the real axis. Therefore, the image of the original fluid domain is now located in the first quarter bounded by the positive real axis and positive imaginary axis. Correspondingly the images of the physical walls are all located along those axes. By adding the symmetrical images of the fluid domain in the three other quarters, the impermeability conditions are straightforwardly satisfied.

As a result of the successive conformal mappings, we have to calculate routinely the image w of a point z in the physical plane, we denote g this mapping function: $z = g(w)$ and the Jacobian of the transformation is the product of the successive conformal transformations:

$$J(w) = \frac{\mathrm{d}z}{\mathrm{d}w} = \frac{\mathrm{d}z}{\mathrm{d}\zeta}\frac{\mathrm{d}\zeta}{\mathrm{d}\zeta'}\frac{\mathrm{d}\zeta'}{\mathrm{d}t}\frac{\mathrm{d}t}{\mathrm{d}w}. \tag{9}$$

All the elementary Jacobians can be formulated analytically, by deriving the expressions (4)–(8). In the sequel the Jacobian J may have as argument either z or w, since $z = g(w)$ implicitly.

It should be noted that the elementary Jacobian $\mathrm{d}\zeta/\mathrm{d}\zeta'$ vanishes at the corners. The elementary Jacobian $\mathrm{d}w/\mathrm{d}t$ also vanishes on the real axis at $w = \pm 1$. That means that the computation of the velocity in the physical domain (even though it is finite at points E or D) requires some care.

Another difficulty may arise when inverting function g, that is to say, calculating z for a given value of w. Eqs. (4)–(8) are easily invertible. Eq. (7) is inverted numerically via a Newton scheme since its derivative is easily computed.

2.2. Adapted Green function

As the transformation is conformal, we still solve Laplace's equation in the final coordinate system. In particular, a Green function which satisfies the boundary conditions is easily derived. These boundary conditions mean that the walls are impermeable and the corresponding Neumann conditions are satisfied by adding images of the Green function with respect to the two axes of the coordinate system.

In practice it is simple when there is no bathymetry since considering a source at ϖ and adding its reflexion[1] at $\overline{\varpi}$ with equal strength, implies that the whole horizontal axis is the support of a homogeneous Neumann condition. In fact it is easy to check that the resulting complex potential

$$F = \log(w - \varpi) + \log(w - \overline{\varpi}), \tag{10}$$

---

[1] The overbar denotes the complex conjugate.

is such that the complex velocity on the horizontal axis $\Im(w)=0$ is real

$$\frac{\mathrm{d}F}{\mathrm{d}z}=\frac{\mathrm{d}F}{\mathrm{d}w}\frac{\mathrm{d}w}{\mathrm{d}z}, \tag{11}$$

where $\mathrm{d}w/\mathrm{d}z$ follows from Eq. (4).

When we consider a bathymetry, it is slightly more complicated. We place sources with equal strength, at the four points ω, $\overline{\omega}$, $-\omega$ and $-\overline{\omega}$. The corresponding complex potential reads

$$F(w,\omega)=\log(w-\omega)+\log(w+\omega)+\log(w-\overline{\omega})+\log(w+\overline{\omega}), \tag{12}$$

$$=\log(w^2-\omega^2)+\log(w^2-\overline{\omega}^2), \tag{13}$$

$$=\log(w^4-2w^2\Re(\omega^2)+|\omega|^4). \tag{14}$$

As a result, the formulation of the Rankine Green function depends on the presence of a bathymetry

$$G(w,\omega)=\begin{cases}\log|w^2-2w\Re(\omega)+|\omega|^2| & \text{no bathymetry,}\\ \log|w^4-2w^2\Re(\omega^2)+|\omega|^4| & \text{with bathymetry.}\end{cases} \tag{15}$$

In the sequel we introduce $X+\mathrm{i}Y$ the complex coordinate of a source in the physical plane which is the image of ω in the transformed plane w through $X+\mathrm{i}Y=g(\omega)$.

2.3. Desingularized technique

The desingularized technique can be now implemented. A finite set of sources are introduced in the physical domain along a curve at a small distance from the actual position of the free surface. There are N sources and their indices are $j\in[1:N]$. The corresponding velocity potential calculated at any point (x,y) in the physical plane and at any instant t, reads

$$\phi(x,y,t)=\sum_{j=1}^{N} q_j(t)G(x,y,X_j(t),Y_j(t)), \tag{16}$$

where (X_j,Y_j) are the location of source number j and q_j is its strength. For the sake of simplicity the time dependency is now omitted. The Green function G follows from

$$G(x,y,X_j,Y_j)=G(w,\omega_j),\quad x+\mathrm{i}y=g(w),\quad X_j+\mathrm{i}Y_j=g(\omega_j). \tag{17}$$

The velocity components (U,V) in the physical plane hence follows from

$$U-\mathrm{i}V=\sum_{j=1}^{N} q_j(t)\frac{\mathrm{d}w}{\mathrm{d}z}\frac{dF}{dw}(w,\omega_j), \tag{18}$$

where the derivative $\mathrm{d}F/\mathrm{d}w$ is simply

$$\frac{\mathrm{d}F}{\mathrm{d}w}=\begin{cases}\left[\dfrac{2w-2\Re(\omega)}{w^2-2w\Re(\omega)+|\omega^2|}\right] & \text{no bathymetry,}\\ \left[4w\dfrac{w^2-\Re(\omega^2)}{w^4-2w^2\Re(\omega^2)+|\omega^4|}\right] & \text{with bathymetry.}\end{cases} \tag{19}$$

2.4. Time marching scheme

The time differential system follows from the continuity of pressure and the velocity written at the moving interface. Both equations must hence be written in a Lagrangian way and they read

$$\begin{cases}\dfrac{\mathrm{d}\phi}{\mathrm{d}t} & = & \dfrac{1}{2}(U^2+V^2)-g(y-h),\\ \dfrac{\mathrm{d}x}{\mathrm{d}t} & = & U,\\ \dfrac{\mathrm{d}y}{\mathrm{d}t} & = & V,\end{cases} \tag{20}$$

where d/dt is the total time derivative, (x,y) are the Cartesian coordinates of the Lagrangian fluid particles or markers always located at the free surface. The time stepping is achieved by using a fourth order Runge–Kutta algorithm. At each intermediate step of the algorithm, the source positions are updated and their intensities as well.

At a given instant t of the resolution, we know $\phi(x,y,t)$ at discrete points (x,y) along the free surface, say (x_i,y_i) the ith point. By using Eq. (16) written at N points (x_i,y_i), we get a linear system whose ith line reads

$$\phi_i = \sum_{j=1}^{N} G_{ij} q_j \quad \text{with} \begin{cases} \phi_i = \phi(x_i, y_i, t), \\ G_{ij} = G(x_i, y_i, X_j(t), Y_j(t)), \end{cases} \tag{21}$$

provided that N sources located at (X_j, Y_j) are introduced. The square matrix with coefficients G_{ij} is denoted $\mathbf{G}$. In practice the position (X_j, Y_j) is determined from the position of the markers (x_j,y_j) and the distance along the local normal direction $\vec{n}$ is simply

$$(X_j, Y_j) = (x_j, y_j) + L_d \vec{n} \quad \text{with } L_d = \delta \frac{L}{N} \text{ and } 1 < j < N. \tag{22}$$

In most computations $\delta = 1$; this arbitrary choice works as long as short time simulations are performed. For longer time simulations, δ can be increased. For very short time simulations, δ can be decreased. More precisely, we may face numerical difficulties when overlapping of sources occurs and when markers (and consequently sources) get too close to each other. The pathology is evident when solving the linear system (21) since two lines become more and more similar and thus the linear system is less and less invertible. Remedies consist in re-gridding the free surface; however, this option is to be avoided as far as possible. As a consequence, we always keep the sources down to the minimum possible provided that conservation laws are checked with the required accuracy.

2.5. *Initial conditions*

At first glance, the present approach offers few possibilities to model an actual Numerical Wave Tank. It is obviously difficult to introduce a moving boundary like a wavemaker or even an absorbing beach. However, this is a difficulty which can be easily circumvented, provided that other approaches, such as the Boussinesq model, can generate realistic distributions of velocity potential and free surface elevation: that is, enough to define initial conditions and start the time differential system (20).

Along these lines tests have been performed on the basis of experiments carried out by Scolan et al. (2007) in the wave flume of Ecole Centrale Marseille. Kinematics in overturning crests are hence computed and compared to experimental data. Small discrepancies are recorded: 5% on the intensity of the velocity, 10% on the direction of the velocity.

Generation of a focused wave is a classical way to achieve steep waves. Recently Bredmose et al. (2010) proceeded that way to simulate flip-through. By tuning the position of the focus point, several wave configurations at the vertical wall can be obtained. They range from air-pocket (or cavity) to run-up without overturning crest. Flip-through occurs at the transition between these two configurations. It should be noted that when gas is entrapped, effects of compressible gas become a significant influence on the time variation of both the local free surface shape and the loads. In this regard computational results are shown in Bredmose et al. (2009). The present model cannot capture those effects. But the same technique used by Zhang et al. (1996) could be implemented.

As a first validation test, we apply the present model to a focused wave. Fig. 2 shows successive snapshots of the wave profile as a focused wave arrives at the left vertical wall. The present model is compared to results based on a "pure" boundary element method developed by Chambarel et al. (2010). The initial condition is generated by the Boussinesq model developed by Kimmoun et al. (2009). This initial state is plotted in the top figure. The wave profiles are then plotted at three other instants: $t = 1.01$, 1.91 and 2.03 s. The wave profiles are identical. There is, however, a remarkable difference between the two numerical approaches, which concerns the required computational resources: CPU-time and memory. For the application illustrated in Fig. 2, the desingularized technique requires 350 markers throughout the time simulation, whereas the standard BEM starts with 260 and ends up with more than 570. It should be also noted that the desingularized method needs neither smoothing nor re-gridding of the free surface. The mass and energy are otherwise conserved with errors less than 0.01% and 0.1%, respectively.

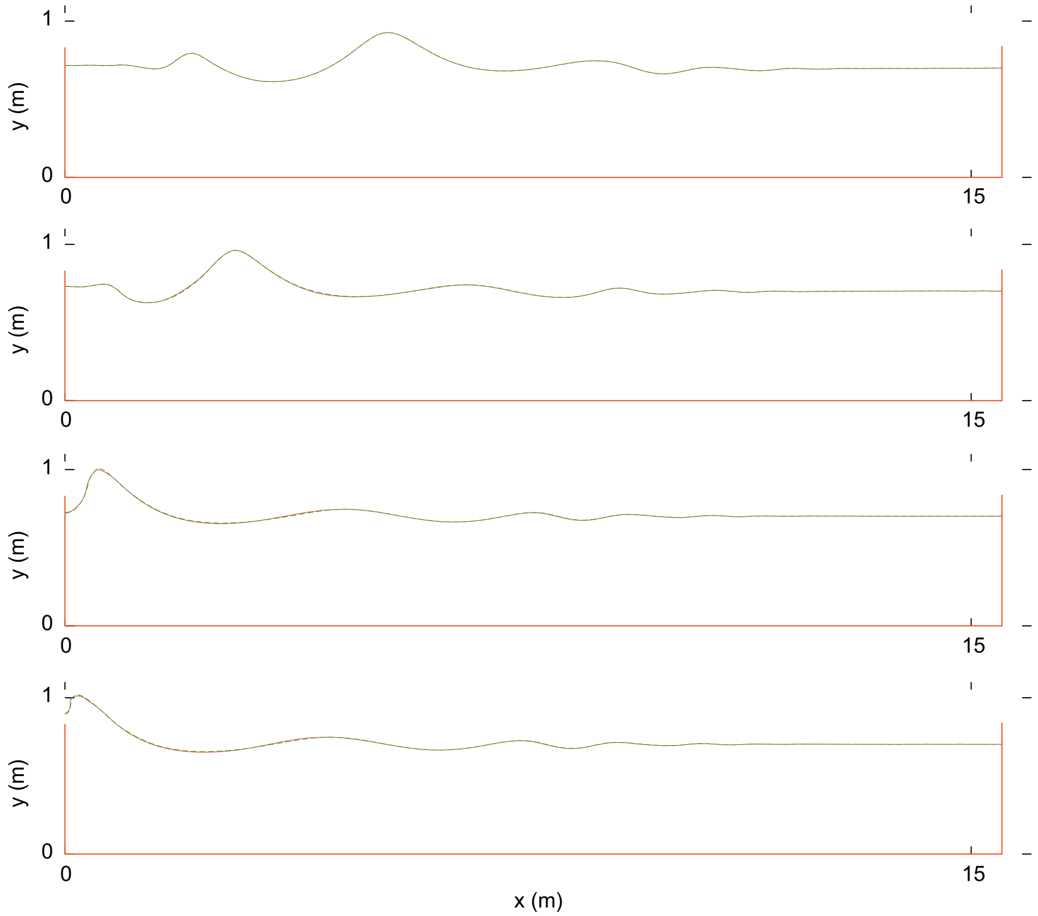

Fig. 2. Comparison of free surface profiles as a focused wave develops at the left vertical wall. The profiles are obtained either with the present method or with a standard BEM developed by Chambarel et al. (2010). The top profile is the initial condition, it is computed with a Boussinesq model developed by Kimmoun et al. (2009). The other three profiles correspond to time $t = 1.01$, 1.91 and 2.03 s from top to bottom.

As an alternative to wave generation based on the initialization with the Boussinesq model, we can model an actual tank in forced motion. Reformulation of the nonlinear free-surface conditions in a moving coordinate system, as done in Faltinsen et al. (2000), is a natural way to study sloshing in a tank. That will be a future application of the present model.

In fact, much computational effort can be saved by adopting another approach. If the purpose is simply the reproduction of flip-through, it is better to shorten the time simulation as much as possible. We can thus (i) avoid numerical instabilities, (ii) diminish the accumulation of numerical errors and (iii) increase the control on the wave configuration of interest.

In the present context, we start with three different types of initial condition. The simplest one is the first sloshing mode of a rectangular basin:

$$y = h - A\cos\left(\frac{\pi x}{L}\right), \quad 0 < x < L, \tag{23}$$

where L is the length of the tank, h is the mean water depth, A is the amplitude of the mode. The shape is defined in a coordinate system where the origin is the bottom left corner. In order to increase the slope of the initial difference in height and therefore improve the control on the transition between air-pocket and run-up, it is better to use either a hyperbolic tangent

$$y = h + A\tanh(R(x-L/2)), \quad 0<x<L, \tag{24}$$

or a part of a Gaussian shape

$$y = h + A\mathrm{e}^{-R(x-L)^2}, \quad 0<x<L, \tag{25}$$

where R controls the slope of the difference in height. The computer program as implemented starts from rest with a given potential energy and a zero kinetic energy. We can calculate the initial potential energy corresponding to each considered shape

$$E_p(0) = \begin{cases} \dfrac{1}{4}\rho g A^2 L, & \text{Eq. (23)}, \\ \dfrac{1}{2}\rho g A^2\left[L - \dfrac{2}{R}\tanh\dfrac{RL}{2}\right], & \text{Eq. (24)}, \\ \dfrac{1}{4\sqrt{2}}\rho g A^2\sqrt{\dfrac{\pi}{R}}\operatorname{erf}(\sqrt{2}RL), & \text{Eq. (25)}. \end{cases} \tag{26}$$

2.6. Conservation of mass and energy

In potential theory and without artificial dissipation, we must check that both mass and energy are conserved. If we denote by $W(t)$ the volume of fluid at any time, we must satisfy the mass conservation law

$$W(t) = \int_{\Omega(t)} \mathrm{d}v = \int_{FS(t)} y\vec{y}\cdot\vec{n}\,\mathrm{d}\ell = \text{constant}, \tag{27}$$

where the inner product times the differential term can be simplified since $\vec{y}\cdot\vec{n} = \mathrm{d}x/\mathrm{d}\ell$. If we consider the time derivative of W, by using (16), we also have

$$\frac{\mathrm{d}W}{\mathrm{d}t} = \int_{FS(t)} \phi_{,n}\,\mathrm{d}\ell = \sum_{j=1}^{N} q_j \int_{FS(t)} G_{j,n}\,\mathrm{d}\ell, \tag{28}$$

where additional simplifications follow from $\vec{x}\cdot\vec{n} = -\mathrm{d}y/\mathrm{d}\ell$. Ideally $\mathrm{d}W/\mathrm{d}t = 0$ by virtue of the Gauss theorem and by recalling that walls are fixed in time. By denoting by E the total energy (kinetic and potential) the energy conservation law reads

$$\frac{\mathrm{d}E}{\mathrm{d}t} = 0, \tag{29}$$

$$E(t) = \int_{\Omega(t)} \left[\frac{1}{2}\rho\vec{\nabla}^2\phi + g\rho(y-h)\right]\mathrm{d}v = \frac{1}{2}\rho\int_{FS(t)} [\phi\vec{\nabla}\phi + g(y-h)^2\vec{y}]\vec{n}\,\mathrm{d}\ell. \tag{30}$$

The integral in (30) can be further turned into a nonlinear quadratic form for q_j. The interest of doing so is limited. In both energy expressions, the integration is performed over the free surface $Fs(t)$ only since the walls are impermeable and fixed in time.

The numerical verifications of $\mathrm{d}W/\mathrm{d}t = 0$ and $\mathrm{d}E/\mathrm{d}t = 0$ are the only way to validate the desingularized techniques applied to nonlinear free surface flows. We have already mentioned the fact that from the initial instant up to numerical divergence mainly due to disconnection[2] of the free surface, we do not disturb the numerical integration, either by smoothing, or by re-gridding. That means that markers are essentially "free to move as they want", and it is worth noting that the markers remain at a reasonable distance from each other and, when they get closer, this concentration of markers occurs in the area where the curvature radius becomes small. On the other hand there is a numerical parameter L_d which is chosen arbitrarily; this is the distance of desingularization. As a consequence, if we enforce either the conservation of mass or the conservation of energy, it is more than likely that we cannot choose L_d as arbitrarily as before. In order to illustrate this incompatibility, numerical tests are performed by coupling the linear system (21) with

---

[2] In the present context, disconnection means that free surface ceases to be a simple continuous line without loop and before impact on any boundary.

the conservation of mass (27). That can be done by minimizing the functional

$$I(q,\lambda)=|\mathbf{G}q-\phi|^2+\lambda|d^{\mathrm{T}}q|, \tag{31}$$

where the two terms of the right hand side are, respectively, the discretized forms of Eqs. (21) and (28) and the superscript $^{\mathrm{T}}$ denotes the transpose of a matrix or vector. The factor λ is a Lagrange multiplier which has no special physical meaning. Minimizing $I(q,\lambda)$ means that its partial derivatives with respect to the components q_i and λ must vanish, yielding

$$\begin{cases} I_{,q_i}=0,\forall i & \Rightarrow\ 2\mathbf{G}\mathbf{G}^{\mathrm{T}}q-2\mathbf{G}^{\mathrm{T}}\phi+\lambda d=0,\\ I_{,\lambda}=0, & \Rightarrow\ d^{\mathrm{T}}q=0. \end{cases} \tag{32}$$

The following linear system is obtained:

$$\begin{pmatrix} 2\mathbf{G}\mathbf{G}^{\mathrm{T}} & d\\ d^{\mathrm{T}} & 0 \end{pmatrix}\cdot\begin{Bmatrix} q\\ \lambda \end{Bmatrix}=\begin{Bmatrix} 2\mathbf{G}^{\mathrm{T}}\phi\\ 0 \end{Bmatrix}. \tag{33}$$

Tests show that solving Eq. (33), whatever the choice of δ, leads rapidly to numerical divergence whatever the discretizations in time or space. As a consequence, if we must constrain the position of the singularities by solving additional equations, desingularized techniques become less attractive, compared to the standard boundary integral equation with collocation points on the actual boundary. Lalli (1997) confirms that the accuracy of the desingularized method depends on a *good choice* of the parameter L_d and this choice depends on the considered applications. That arbitrariness offers some perspectives since we know that errors are unavoidable.

2.7. The role of an additive constant in the velocity potential

We introduce an arbitrary additive function of time $a(t)$ to the velocity potential. By definition, its time derivative can be considered as the Bernoulli constant. By performing numerical tests, it appears that constant $a(t)$ plays a role in the computations.

Mathematically its influence is clear when the geometry is simple. However, from the literature the role of $a(t)$ is still an open problem. From the mathematical point of view, Christiansen (1976) reports that $a(t)$ avoids the non-uniqueness of the solution. However, in the present case we know that ϕ is defined with an additive function of time. Bogomolny (1985) minimizes its influence on the accuracy but ends up with the paradoxical conclusion: the higher the distance between the actual contour and the singularities line, the better the approximation. Pozrikidis (2000) examines in which circumstances the constant must be retained or not; that depends on the existence of a vanishing eigenvalue of the single-layer operator (source distribution on the contour which encloses the whole fluid domain). Goldberg (1995) mentions its dependence on the geometry of the computational domain. By introducing this constant as a normalization factor Mathon and Johnston (1977) mention its role in the acceleration of the convergence when the locations of the singularities are a part of the solution. Smyrlis and Karageorghis (2001) compare the condition numbers (ratio of the smallest to the highest eigenvalues) of the matrices to invert with $a(t)\neq 0$ or $a(t)=0$. No improvements are observed when the geometry is a disk. Here the considered problem is slightly more complicated since the positions of the singularities vary in time and we expect a strongly irregular line along which singularities are placed (overturning crest, local jet like flip-through, *etc.*). That is the reason why we pay great attention to this arbitrary choice and we quantify its influence on conservation laws.

In practice we introduce $a(t)$ in Eq. (16) yielding the following algebraic form:

$$\phi_i=\sum_{j=1}^{N}G_{ij}q_j(t)+a(t). \tag{34}$$

This constant can be written as a factor times the source strength summation, say

$$a(t)=b\sum_{j=1}^{N}q_j(t), \tag{35}$$

where b does not depend on time (and obviously not on space either). In practice we invert the matrix $\mathbf{G}+b\mathbf{1}$ instead of $\mathbf{G}$ alone. All coefficients of matrix $\mathbf{1}$ are unity. That means the conditioning of the inverted matrix is modified. In fact it is worth recalling what are the properties of the matrix $\mathbf{G}$. We consider the Dirichlet problem formulated within a standard boundary element method. The corresponding integral equation reads

$$\phi(P) = \int_{\partial\Omega} G(P,Q)q(Q)\,\mathrm{d}\ell. \tag{36}$$

If we evaluate the contribution of the singularity when $P \rightarrow Q$, we clearly know that it is zero. That is the reason why this problem, yielding a Fredholm equation of the first kind, is ill-conditioned since the diagonal of the resulting matrix is not dominant. Actually Eq. (36) is not solved. As an alternative the integral equation obtained by taking the normal gradient of Eq. (36) is solved. In the present context, the problem is completely different since the source approaching the actual free surface may lead to a high value on the diagonal. The singularity grows like Log L_d. By introducing a constant $a(t)$, we add the constant b to each coefficient of the matrix to be inverted. Numerical experiments show that the constant b has an influence on the duration of the simulation and on the conservation laws. As a criterion of the accuracy of the numerical inversion, we systematically evaluate the number of exact digits during the resolution. An easy way is to use a Gauss algorithm with an additional right hand side made up of the summation per line of the coefficients of the matrix to be inverted; the solution must be unity uniformly. The discrepancy with unity should be of the order of the precision of the processor used, here 10^{-15}.

We illustrate the role of constant b by computing the inverse matrix $(\mathbf{G}+b\mathbf{1})^{-1}$ of Eq. (21)). We test the algorithm with the initial condition (24). The simulation runs over 47 time steps $\Delta t = 0.01$ s and a space discretization is defined by 150 equally distributed markers along the free surface line at the initial time. The simulation runs over 48 time steps after which the case $b = 0$ stops due to numerical divergence. The global comparisons done in Fig. 3 on the free-surface profiles, do not show noticeable differences at each computed time step, at least where the free surface is highly disturbed. The profile of the inverse matrice $(\mathbf{G}+b\mathbf{1})^{-1}$ computed at instant $t = 0.47$ s, is drawn in Fig. 4. The diagonal coefficients are drawn as well. The comparisons done show that differences are hardly noticeable at least where the coefficients reach their highest value. It is worth noting that we can ideally check the following identity

$$(\mathbf{G} + b\mathbf{1})^{-1} = \mathbf{G}^{-1}, \tag{37}$$

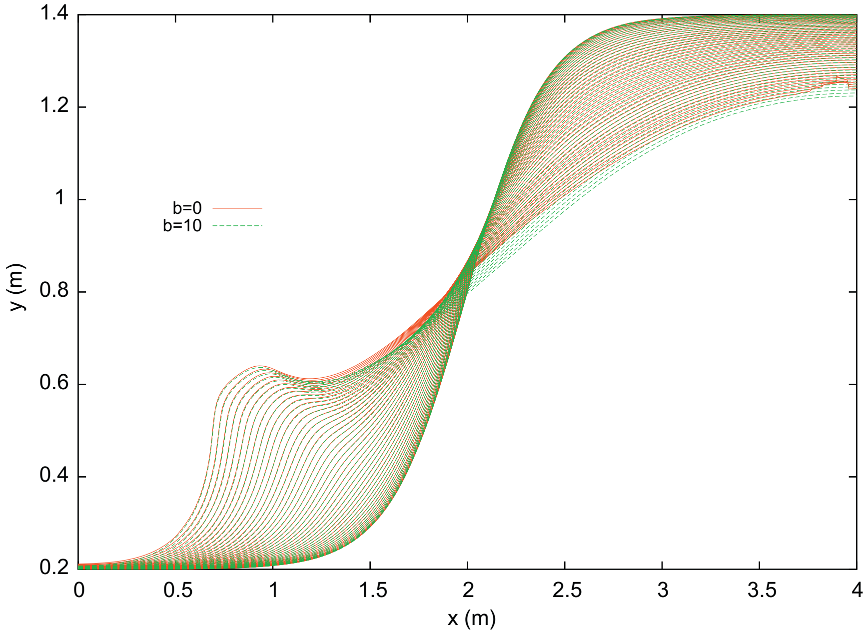

Fig. 3. Free-surface profiles computed with the initial condition defined by Eq. (24) and parameters $A = 0.6$ m, $h = 0.8$ m, $R = 2.5$, $L = 4$ m. One over two profiles is plotted. Comparison of two computations: $b = 0$ and 10.

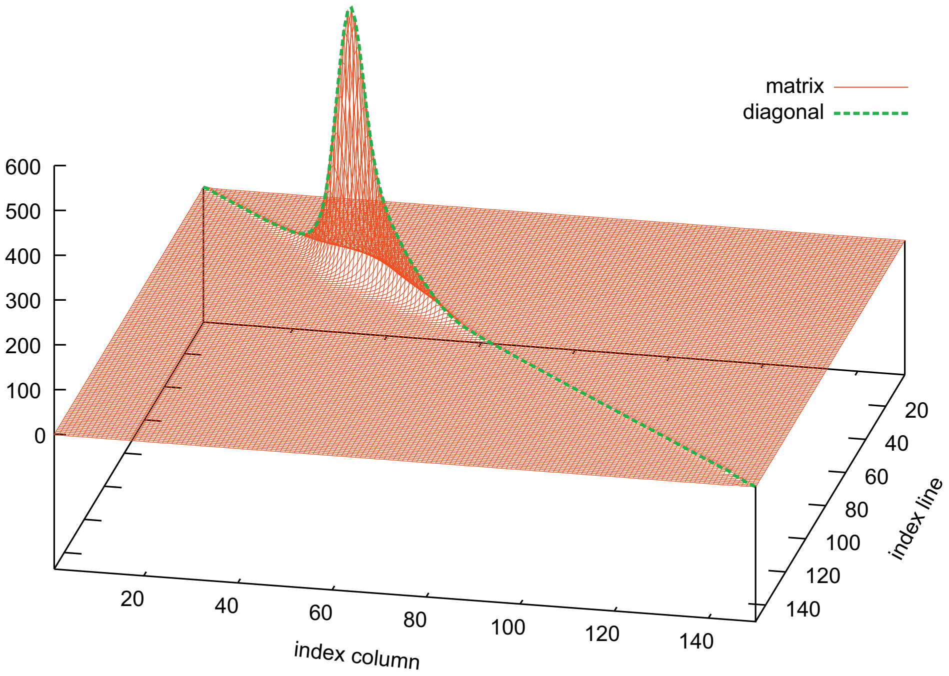

Fig. 4. Profiles of the inverse matrices $(\mathbf{G}+b\mathbf{1})^{-1}$ computed at $t = 0.47$ s for either $b = 0$ or 1000. The initial condition is defined in the caption of Fig. 3. The absolute value $|(\mathbf{G}+b\mathbf{1})^{-1}_{ij}|$ is plotted in terms of indices (i,j). The diagonal coefficients $|(\mathbf{G}+b\mathbf{1})^{-1}_{ii}|$ are superimposed.

if the summation of the coefficients of **G** by column is zero, *i.e.*

$$\sum_{i=1}^{N} G^{-1}_{ij} = 0, \quad \forall j = 1,\ldots,N. \tag{38}$$

The identity (37) is proved by multiplying both sides with $\mathbf{G}+b\mathbf{1}$. This is a theoretical result and it is not certain that we can prove that condition (38) can be necessarily checked regarding our boundary value problem. Paradoxically if condition (38) is fulfilled, it would mean that the problem is highly ill-conditioned since this condition precisely means that the lines of matrix **G** are not linearly independent. The main result is: using a nonzero constant b, we enforce condition (38), and we can even show that the sum of the coefficients of **G** by line is low as well. In practice we obtain the result

$$\sum_{i=1}^{N} (G+b\mathbf{1})^{-1}_{ij} < \frac{M}{|b|}, \quad \sum_{j=1}^{N} (G+b\mathbf{1})^{-1}_{ij} < \frac{M'}{|b|} \quad \text{with } M>0 \text{ and } M'>0, \tag{39}$$

which can be easily proved. As an illustration the quantities in Eq. (39) are plotted in Fig. 5. It is worth noting that disturbances appearing when $b = 0$ at nodes ≈ 140 (on the right side), disappear as soon as $b>0$. Disturbances are necessarily correlated to a sudden short distance between two successive markers. Fig. 6 shows the time variation of this distance; the shortest distance is obtained precisely at node #146. The connection between condition (39) and conservation laws (28) and (30) is difficult to establish, but, from numerical experiments, we can show that the effects of a nonzero constant b seem to inhibit the development of numerical disturbances. For the same application case we plot in Fig. 7 the time variation of the discrepancies on the conservation of mass and energy. Improvements due to $b \neq 0$ are clear.

The factor b is not the only parameter which influences the numerical scheme and the conservation laws. The next section analyses more deeply the combined effects of factor b and the desingularizing distance L_d.

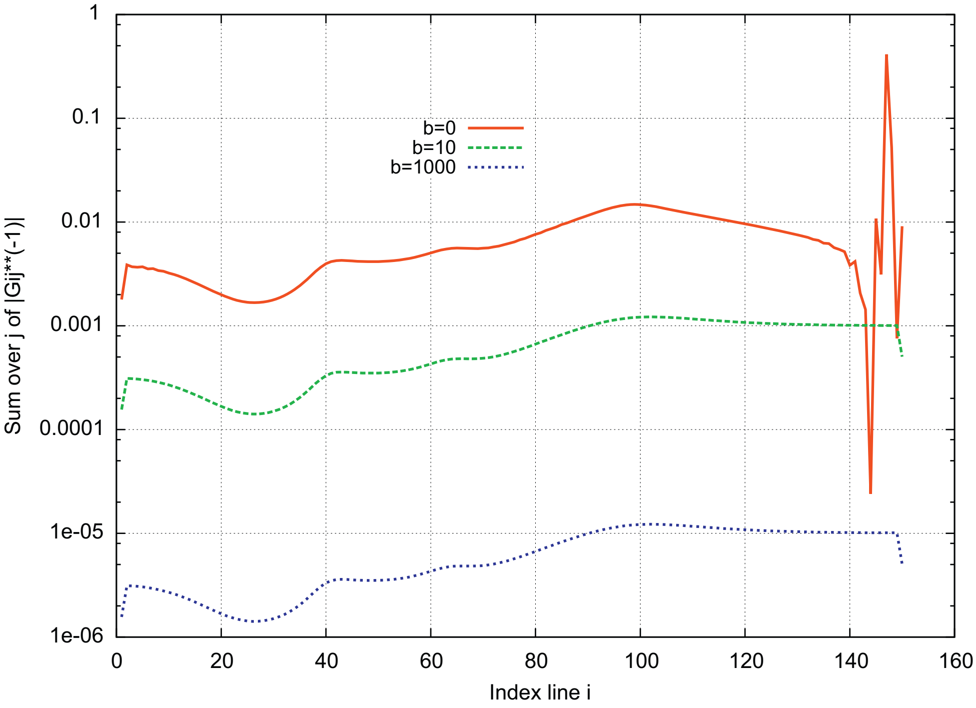

Fig. 5. Variation of the sum of the coefficients of $(\mathbf{G}+b\mathbf{1})^{-1}$ by line at $t = 0.47$ s for three values of $b = 0, 10, 1000$. The initial condition is defined in the caption of Fig. 3. Disturbances appear for $b = 0$ about node 146.

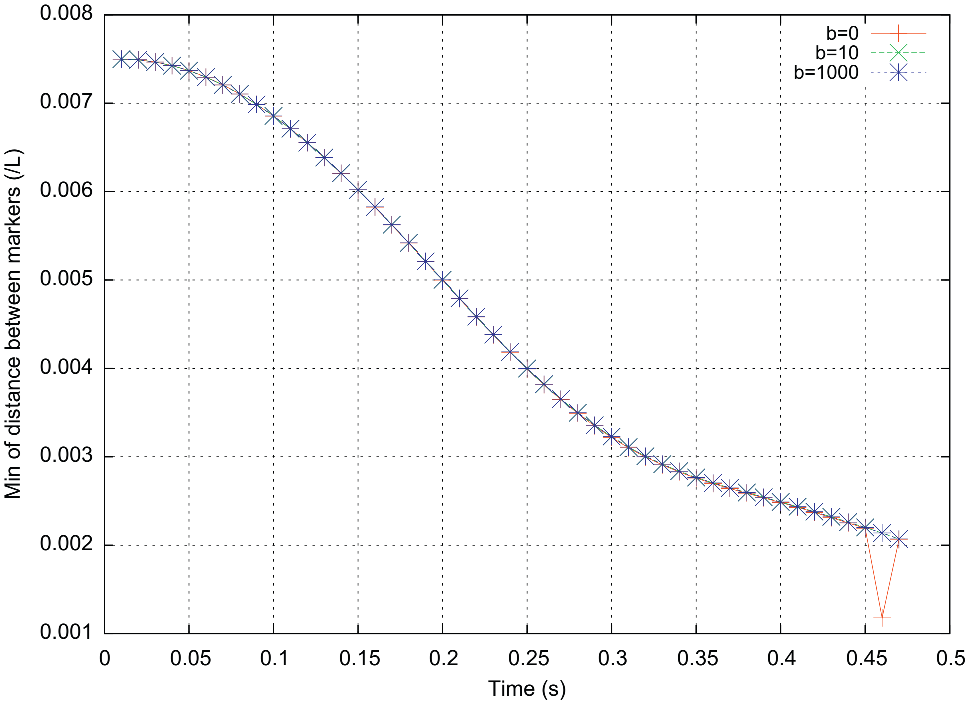

Fig. 6. Time variations of the minimum distance between two successive markers for three values of $b = 0, 10, 1000$. The initial condition is defined in the caption of Fig. 3. For $b = 0$, the smallest distance is reached at node 146.

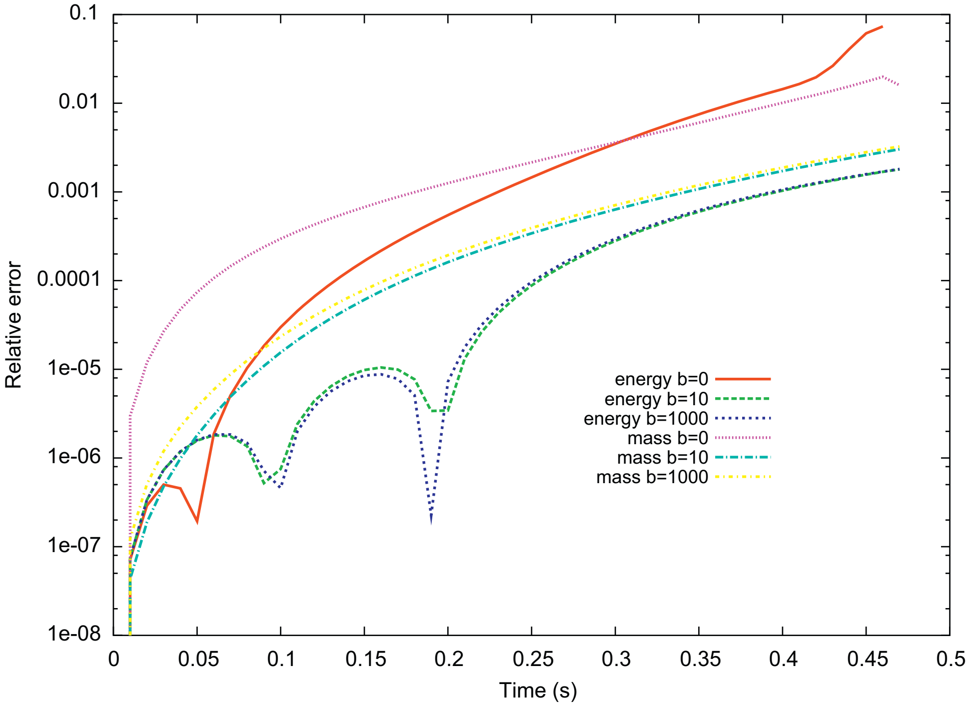

Fig. 7. Time variation of the relative error on conservation laws: mass and total energy for three values of $b = 0$, 10 and 1000. The initial condition is defined in the caption of Fig. 3.

2.8. The role of the desingularizing distance

In order to justify our choice of L_d, we consider two examples. The first concerns the weakly nonlinear case and we start with the first sloshing mode of a rectangular basin (see Eq. (23)). If the amplitude A is low enough, the simulation can last endlessly. Results are obtained with $A = 0.2\,\text{m}$, $h = 0.75\,\text{m}$ and $L = 4\,\text{m}$. Fig. 8 shows the time variation of the free surface elevation at left intersection with the vertical wall when $\delta = 1$ and values of b varying in the range $b \in [0 : 10\,000]$. Whatever the value of b the results for these long simulations are quite similar except for $b = 0$ for which slight differences appear after a while (say $t > 2.5\,\text{s}$). Fig. 9 illustrates the influence of δ while b is set to a constant $b = 1000$. Main discrepancies appear when $\delta < 1$ except at the early stage of the fluid motion (here up to $t = 1.2\,\text{s}$). In the present application, it is observed that δ cannot be greater than 3, otherwise the simulation stops prematurely. The time variations of the different quantities $W(t)$ from Eq. (27) and $E(t)$ from Eq. (30), while parameters L_d and b vary, are compared as well. The influences of both parameters δ and b appear clearly. This confirms the fact that δ cannot be lower than 1 and b must be high enough to be sure that discrepancies on mass and energy conservation are reasonable, that is to say below 1%. In the present case b must be greater than 1000. Figs. 10 and 11 sum up the results in terms of the standard deviation of the relative error with the theoretical result, that is to say perfect conservation of mass and energy. It should be noted that the standard deviation for $\delta = 3$ is calculated over a much shorter duration than other cases. These results confirm the preponderant influence of δ on the conservation laws at least for this weakly nonlinear application.

However, when the liquid motion becomes highly nonlinear, disconnection of the free surface or overturning crests occur rapidly and the duration of a simulation becomes much shorter. As an illustration, we consider the initial condition defined by a first mode of the rectangular tank (see Eq. (23)) but with a higher initial amplitude $A = 0.4\,\text{m}$. Fig. 12 shows the corresponding free surface profiles as the crest develops for the two values $\delta = 1$ and 1.6. It is shown in the present case that δ must be greater than 1 (in fact $\delta = 1.6$) in order to get the best compromise combining a long enough simulation and the best conservation of mass and energy.

We next consider the fluid motion resulting from the initial condition (24). This case is of great interest since it will provide the initial conditions of the flip-through. The initial amplitude is $A = 0.495\,\text{m}$, the mean liquid level is $h = 0.75\,\text{m}$ and the length of the tank is $L = 4\,\text{m}$. The highest slope is located at the middle of the tank and it is tuned

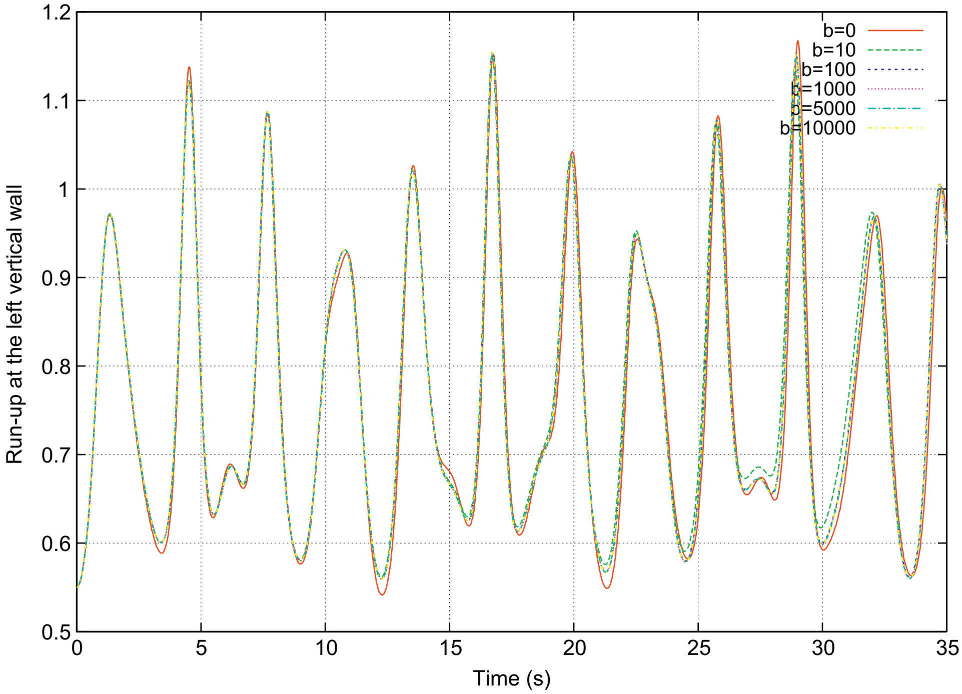

Fig. 8. Time variations of the free surface elevation at the left vertical wall. The initial condition is defined by Eq. (24) and parameters $A = 0.2\,\mathrm{m}$, $h = 0.75\,\mathrm{m}$, $R = 2.4$ and $L = 4\,\mathrm{m}$. $\delta = 1$ and b is variable.

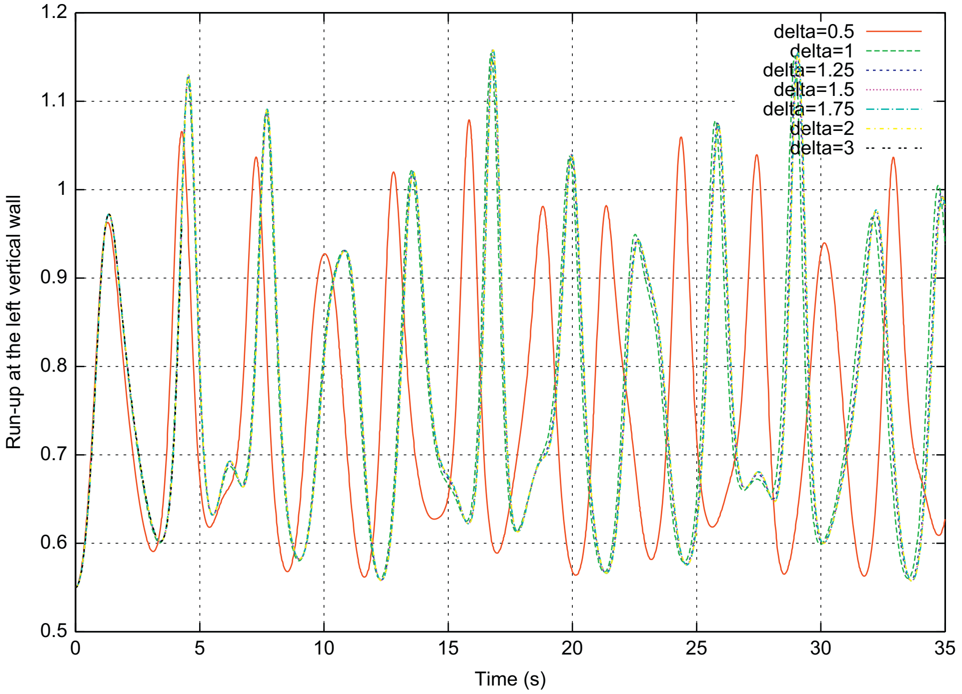

Fig. 9. Time variations of the free surface elevation at the left vertical wall. The initial condition is defined in the caption of Fig. 8. $b = 1000$ and δ is variable.

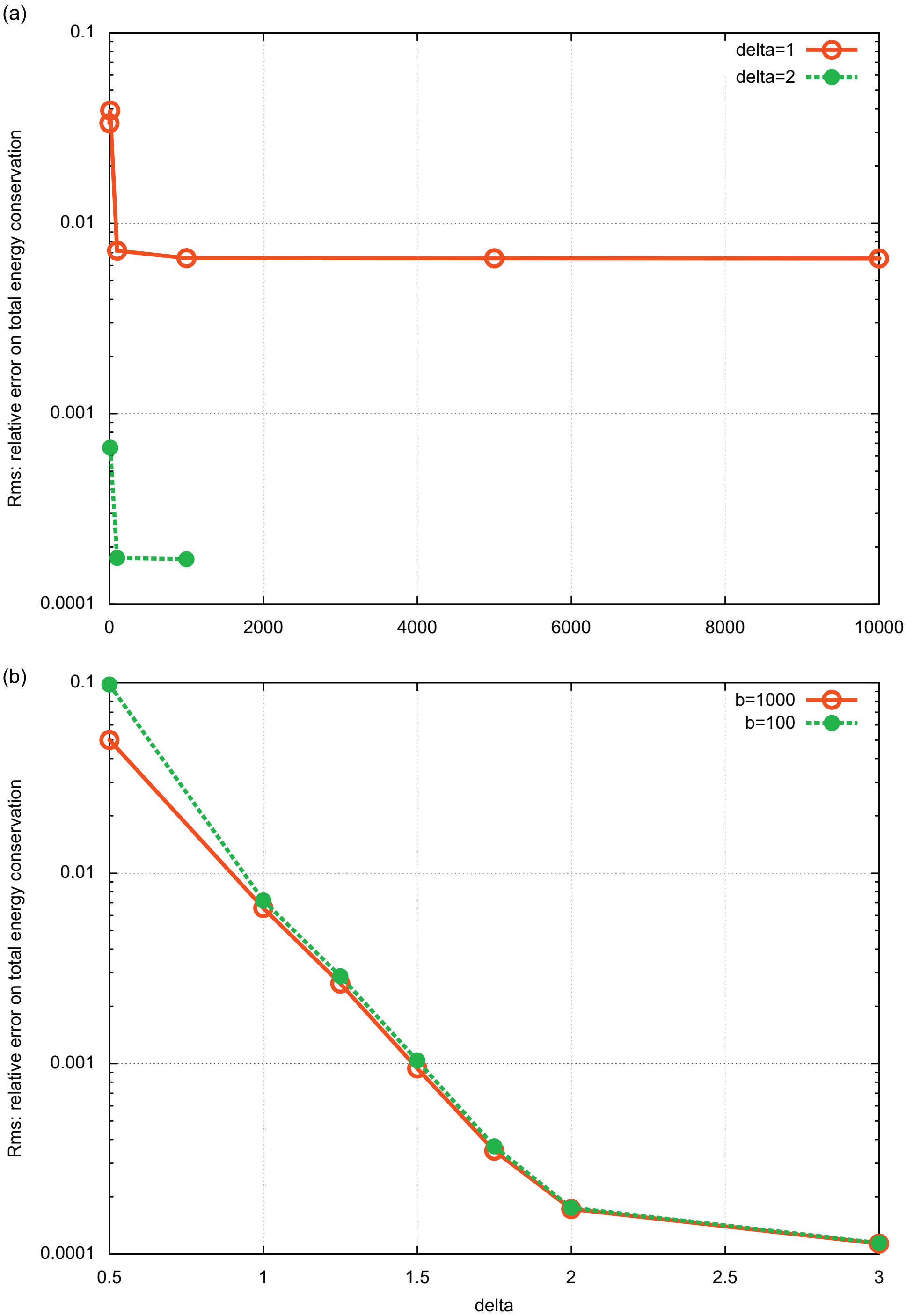

Fig. 10. Standard deviation of the relative error on the total energy conservation, for varying parameters b (*top*) and δ (*bottom*). The initial condition is defined in the caption of Fig. 8.

with the coefficient R, here $R = 2.4$. We test different desingularizing distances varying in the interval $\delta \in [0.5 : 2]$. The constant b is set to $b = 1000$ which is high enough to improve the mass and energy conservation. Fig. 13 shows the computed free surface profile at a given instant $t = 0.62\,\mathrm{s}$ as the parameter δ varies. Over the whole length of the tank, we observe wide discrepancies between $\delta = 0.5$ on one side and $\delta > 1$ on the other side. Only slight discrepancies occur

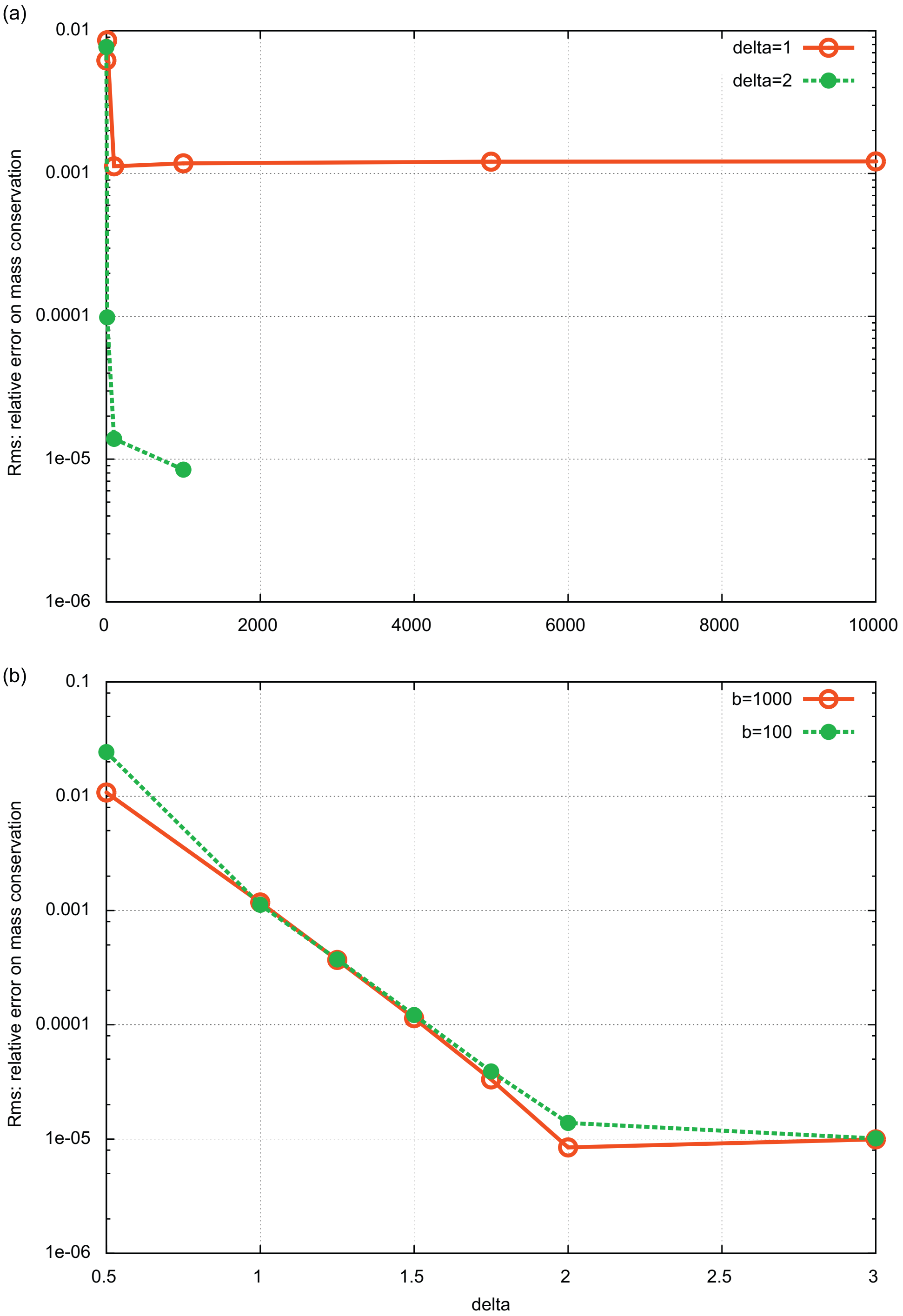

Fig. 11. Standard deviation of the relative error on the total mass conservation, for varying parameters b (*top*) and δ (*bottom*). The initial condition is defined in the caption of Fig. 8.

for the different considered values of $\delta > 1$. It should be noted that these differences seem to occur mainly in the right hand side of the tank and not where the crest starts overturning on the left hand side.

Time variation of relative errors on energy and mass are plotted in Figs. 14 and 15, respectively. Here again, the numerical tests confirm that δ must be greater than or equal to unity in order to get reasonable conservations of both

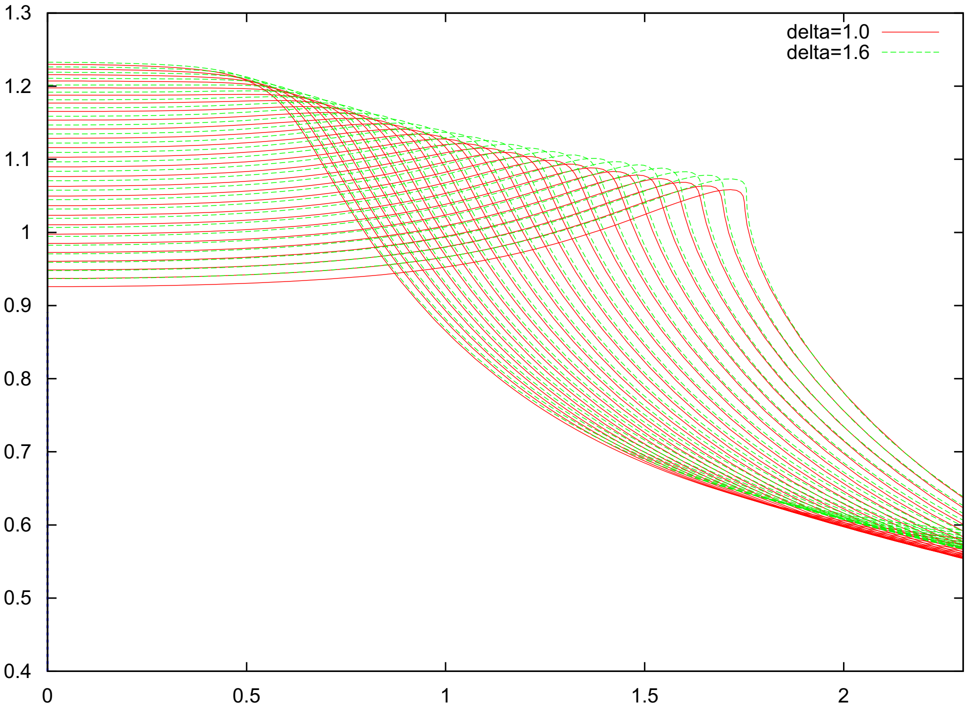

Fig. 12. Free surface profiles when $t > 1.3$ s, with $\delta = 1$ and 1.6. The initial condition is defined by Eq. (23) and parameters $A = 0.4$ m, $h = 0.75$ m, $R = 2.4$ and $L = 4$ m.

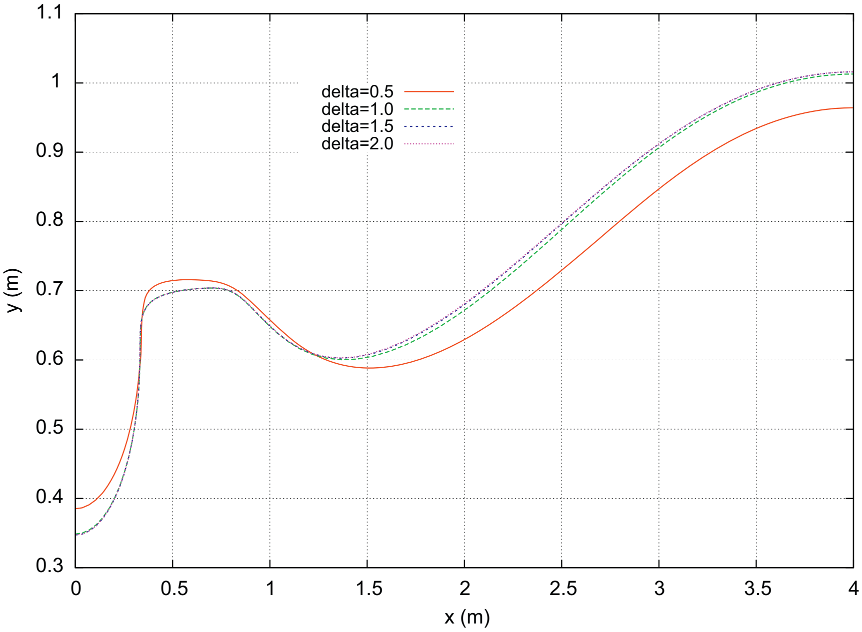

Fig. 13. Free surface profiles computed at $t = 0.62$ s for varying values of $\delta \in [0.5 : 2]$. The initial condition is defined by Eq. (24) and parameters $A = 0.495$ m, $h = 0.75$ m, $R = 2.4$ and $L = 4$ m.

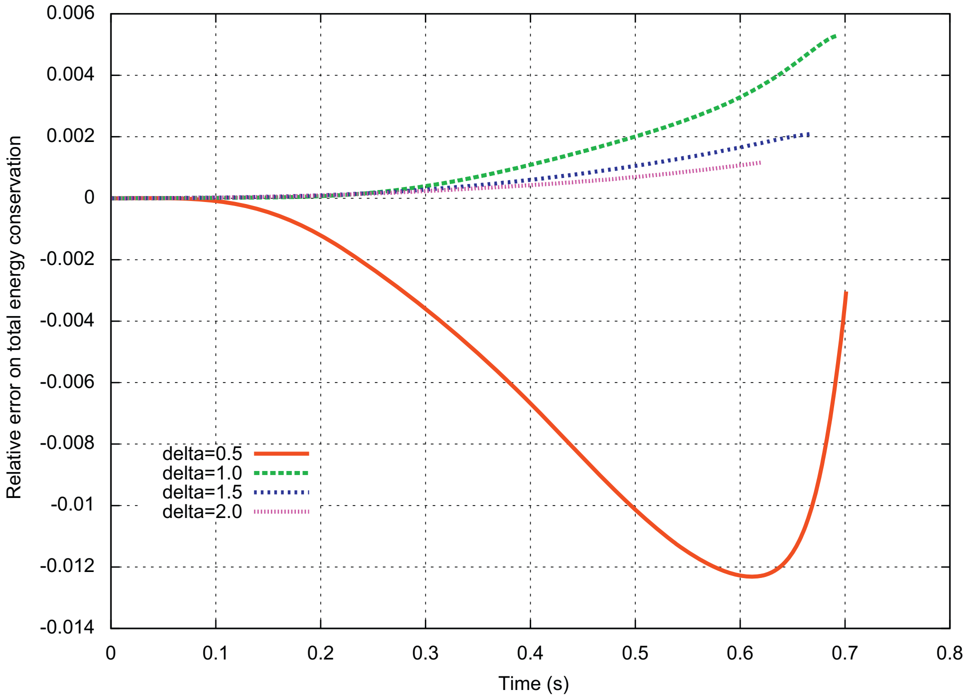

Fig. 14. Time variations of the relative error on the energy conservation for $b = 1000$ and varying parameter $\delta \in [0.5 : 2]$. The initial condition is defined in the caption of Fig. 13.

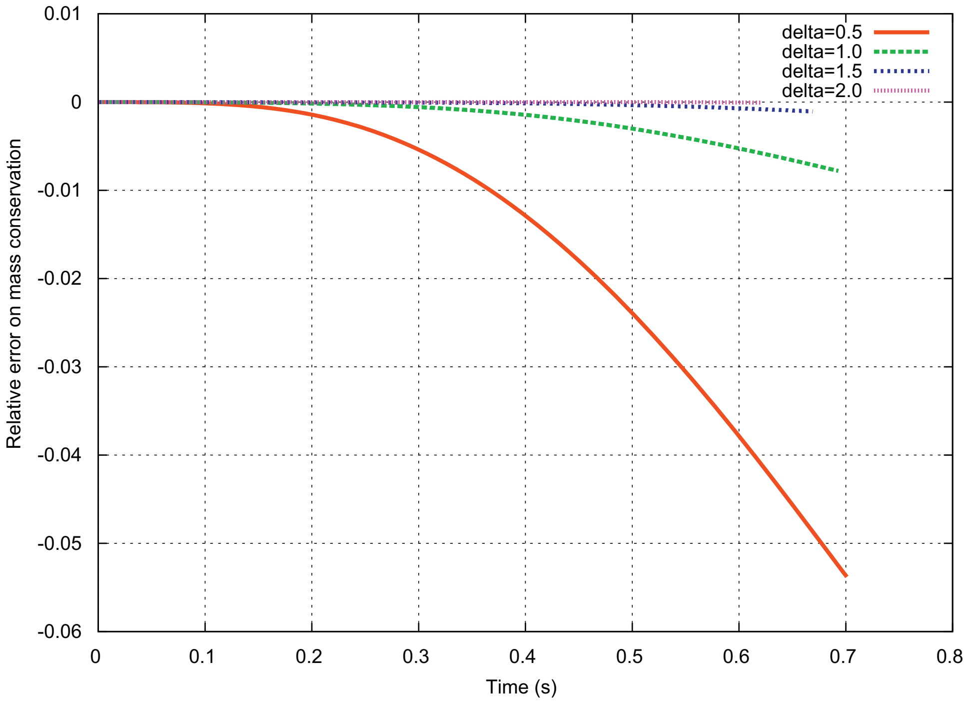

Fig. 15. Time variations of the relative error on the volume $W(t)$ for $b = 1000$ and varying parameter $\delta \in [0.5 : 2]$. The initial condition is defined in the caption of Fig. 13.

mass and energy. However, when $\delta > 2$, numerical divergence may occur, thus shortening the duration of the simulation. In the present case $\delta = 1$ is indeed the best compromise between stability and accuracy.

3. Some features of the flip-through phenomenon

We aim to examine some aspects of the flip-through phenomenon. Experimental observations show that its occurrence corresponds to a transition between the formation of an air-pocket (or cavity) and a smooth run-up along the wall. The typical computed free surface profiles are plotted in Fig. 16 starting from the initial deformation given by Eq. (24). The obtained wave kinematics is quite similar to the kinematics of a soliton riding on a gently sloping beach. If the fluid depth can be roughly approximated as $h = 0.75\,\mathrm{m}$, then the typical velocity of the front is $\sqrt{gh} = 2.7\,\mathrm{m/s}$ and the front arrives at the wall within the time interval of $\delta t \approx 0.7\,\mathrm{s}$. A critical profile is identified at the last stages of the flow. Cooker (2010) showed that changes of concavity occur precisely when the local free surface profile has the parabolic feature illustrated in Fig. 16. At that stage, there is a competition between the more or less fast run-up and the nascent wave crest. As a consequence we observe that the velocity along the vertical wall and the velocity at the vertical wave front (where the slope is nearly vertical) have quite similar amplitudes. The same observation has been experimentally made by Lugni et al. (2006).

3.1. Parametric study

A parametric study is performed in order to identify some pairs of parameters (A,h) of interest. Two criteria are retained: (i) fast run-up along the vertical wall and (ii) appearance of a significant peak pressure. By tuning the amplitude A, we can progressively observe all the possible configurations ranging from a mild run-up to an entrapped air pocket. It is clear that the present model cannot capture the influence of the entrapped air pocket. Faltinsen and Timokha (2009) provide suitable models.

Figs. 17 and 18 illustrate two clearly different cases bounding the range of A in which we can simulate flip-through. The only varying parameter is the amplitude A of the initial deformation. Figs. 17 and 18 show the ultimate stages of the flow as the wave arrives at the left vertical wall. For each free surface profile, the corresponding pressure distribution along the vertical is plotted as well. The superimposed curve follows the maximum of pressure of each instantaneous pressure distribution.

When $A = 0.4\,\mathrm{m}$, we observe a standard run-up for which the pressure hardly goes above 170 mbar. The free surface does indeed flip along the wall, but no jet is observed. When $A = 0.54\,\mathrm{m}$ on the contrary, a gas pocket appears. That does not keep the pressure increasing continuously, as fluid impact on the wall is likely to occur before any maximum of pressure is reached. On the other hand, entrapped gas modifies the loads most probably.

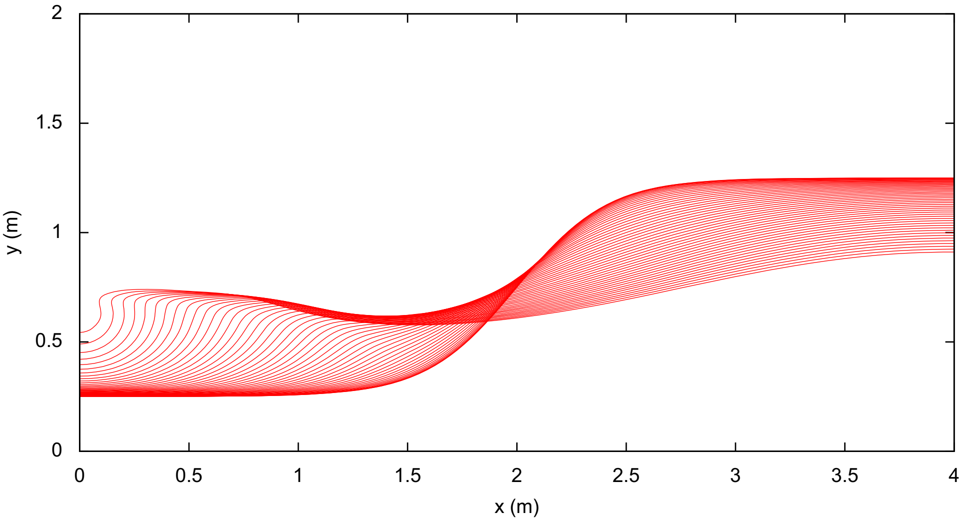

Fig. 16. Wave profiles during a standard simulation. The initial condition is of type (24). Simulation of a parabolic free surface shape at the left vertical wall.

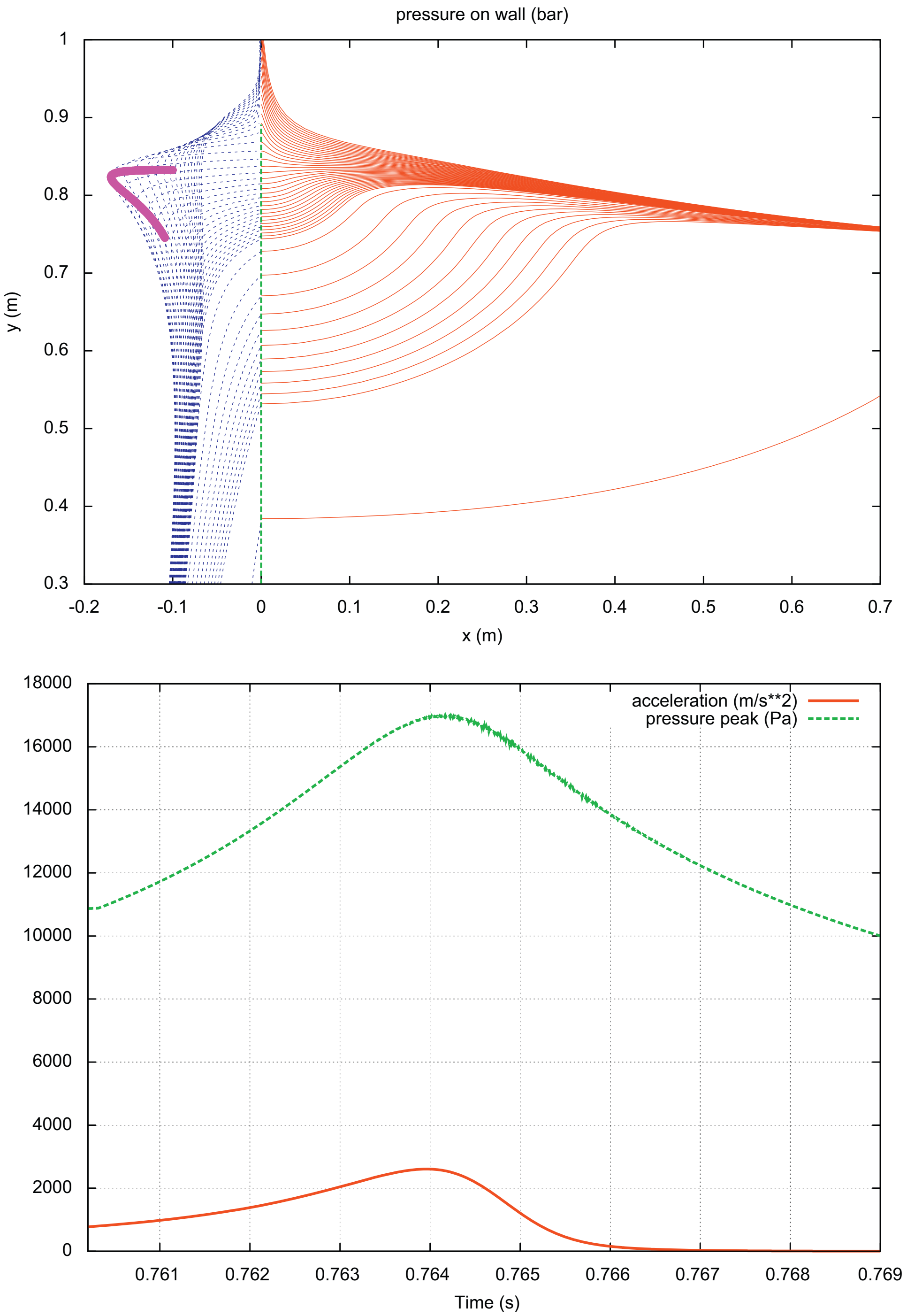

Fig. 17. In *top* figure: distribution of pressure on the left vertical wall (*left*) and corresponding free surface profile (*right*). The superimposed curve follows the peak of each pressure distribution as soon as the pressure becomes higher than hydrostatic pressure on the bottom. In *bottom* figure: time variations of the acceleration of the left intersection of free surface with the vertical wall. The initial condition is defined by Eq. (24) and parameters $A = 0.4\,\text{m}$, $h = 0.75\,\text{m}$, $R = 2.4$ and $L = 4\,\text{m}$.

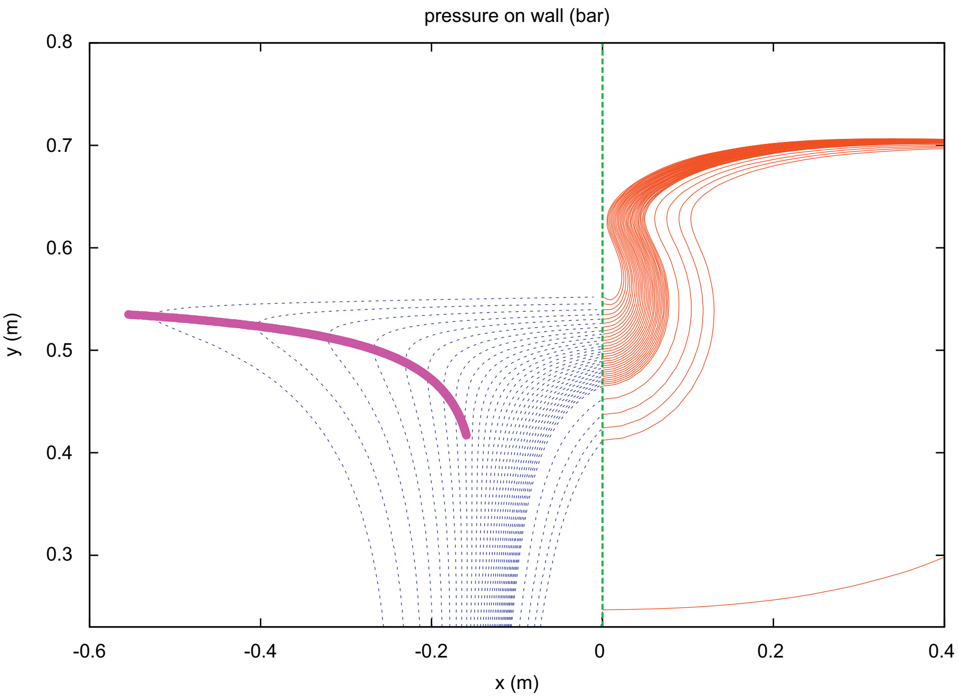

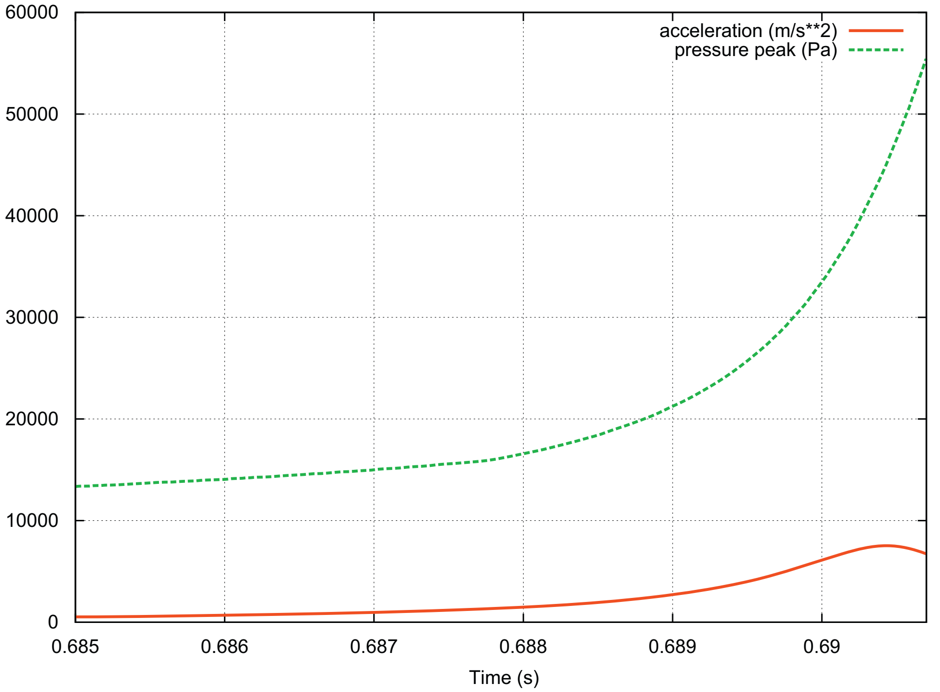

Fig. 18. See Fig. 17 for explanation. The initial condition is defined by Eq. (24) and parameters $A = 0.54\,\mathrm{m}$, $h = 0.75\,\mathrm{m}$, $R = 2.4$ and $L = 4\,\mathrm{m}$.

When flip-through is expected, the local curvature radius can become very low. At the last stage of the flow—flip through is starting and very small curvature radii are expected—the corresponding desingularizing distance becomes too high to prevent intersection of the sources line with the actual boundaries (wall or free surface itself). We can increase the number of markers, but that increases numerical instabilities as well. As noticed by Tuck (1998), the desingularizing distance must be adapted. However, as shown earlier the consequences are that we disturb the conservation laws.

3.2. Numerical adaptation to capture highly distorted free surface

In order to pursue the simulation the only way is to decrease as much as necessary the desingularizing distance locally where curvature radii are low. In order to smoothly decrease L_d in the close vicinity of the wall, the following formula is proposed

$$L_d = \delta \frac{L}{N}(1-\gamma e^{-4s/L}), \tag{40}$$

where s denotes the curvilinear abscissa along the free surface measured from the left vertical wall. The numerical tests show that $\delta = 1$ and $\gamma = 0.8$ in formula (40) makes it possible to continue the simulation far enough and even when the jet starts riding along the wall. As a first numerical test, we start with the same initial condition as in Fig. 17. The amplitude of the initial difference in height is $A \approx 0.52$ m, the slope at the mid tank is set by $R = 2$, the length is $L = 4$ m and the mean water level is $h = 0.75$ m. We use 155 markers uniformly distributed along the free surface line at the initial time. The time step is set to $\Delta t = 0.005$ s and it is substantially decreased when $t \geq 0.68$ s with the consequence that some computed quantities may have time discontinuities at that instant. In the meantime, at instant $t = 0.665$ s, the

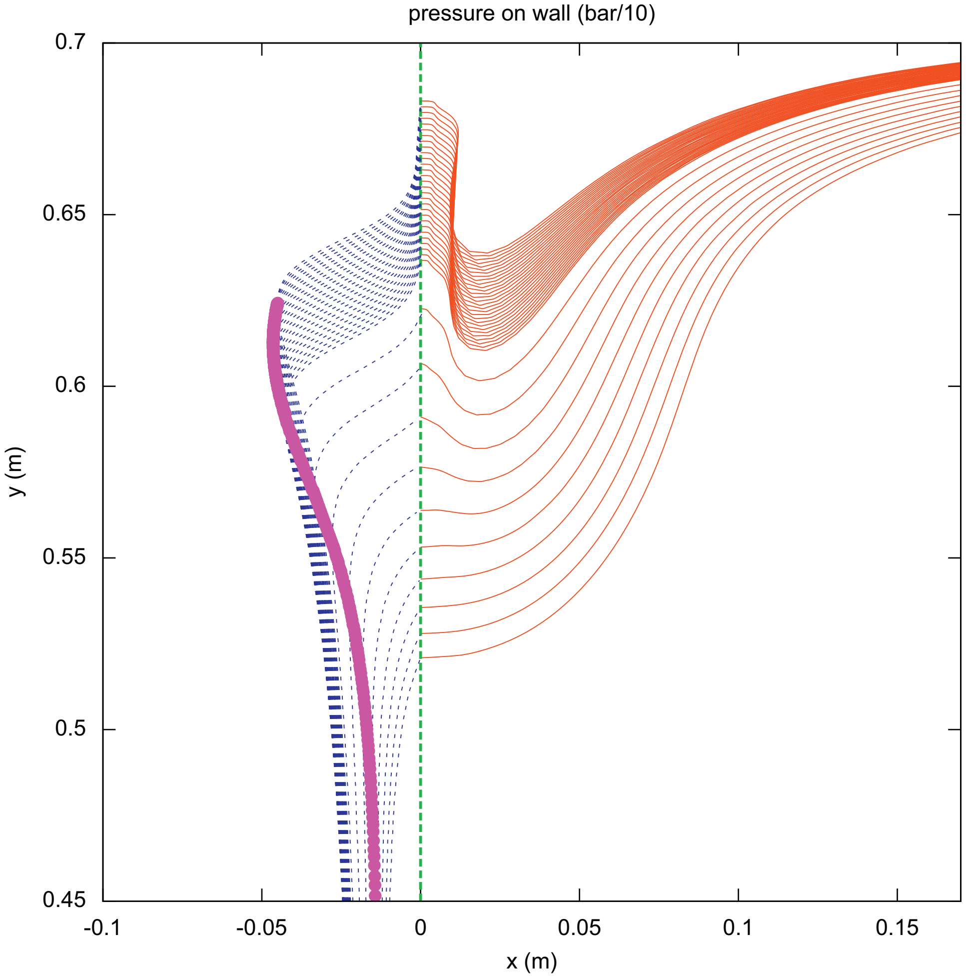

Fig. 19. See Fig. 17 for explanation. The pressure in bar in divided by 10. The initial condition is defined by Eq. (24) and parameters $A = 0.52$ m, $h = 0.75$ m, $R = 2$ and $L = 4$ m.

source line is modified according to formula (40). Fig. 19 shows the pressure profiles and the corresponding free surface profiles at some instant before and after the flip-through occurrence. Fig. 20 shows the results concerning the energy and mass conservation. A clear discrepancy for energy is noticeable at the end of the simulation but both are conserved satisfactorily. Fig. 21 sums up the results concerning the kinematics and the corresponding loads. The present case is denoted by (tanh) since it corresponds to an initial hyperbolic tangent free surface deformation.

The time variation of the pressure peak is plotted and it can be compared to the time variation of the acceleration of the tip of the rising jet. The maximum pressure (here about $P_{\max} = 0.4$ bar) is reached at time $t \approx 0.6918$ s and follows the instant at which the acceleration reaches its maximum at time $t \approx 0.6859$ s. Fig. 21 also show the time variation of the positions along the left vertical wall of pressure peak $y_{p_{\max}}$ and the intersection point $y_{x=0}$. The minimum distance between the two points $y_{p_{\max}}$ and $y_{x=0}$ occurs in the time interval between the maximum acceleration and the maximum of pressure occurrences. This observation differs from those of Cooker (2010) for whom the maximum of pressure peak occurs before the maximum of acceleration. Longuet-Higgins (2001) suggests in contrast that these two maxima are concomitant. This concomitancy seems rather connected to a standard run-up configuration as illustrated in Fig. 17. It is indeed observed that maximum of pressure and maximum of acceleration occur at precisely the same instant.

3.3. *Influence of initial conditions on flip-through*

In order to confirm the observed chronology, we start with another initial condition. Instead of a hyperbolic tangent, we start with a half gaussian defined by Eq. (25). We choose $L = 4$ m, $R = 0.5\,\mathrm{m}^{-2}$ and $A = 1$ m, hence the initial energy is of similar order as for the case studied earlier. We can then compare the influence of the shape of the initial deformation. Fig. 22 shows the free surface profiles—whatever the instants at which the profiles correspond—for an initial shape of type (24) and of (25). For the sake of comparison, we adjust the origin in the vertical direction so that the flip occurs roughly at the same vertical position. Fig. 22 shows a general view and a zoom locally as the jet develops. In fact we cannot distinguish clear differences between the two configurations when the free surface flips at the wall, whereas the fluid flows elsewhere are clearly different.

That is confirmed by examining other results such as the time variations of maximum of pressure and the kinematics of the rising jet. They are plotted in Fig. 21. They are denoted by (gauss) in order to be compared to the previous results when starting from an initial hyperbolic tangent free surface deformation. The same time lag $\delta t = 0.2931$ s is imposed on all time histories so that we can surprisingly observe a reasonable superimposition of each signal. That confirms that flip-through does not depend much on the type of initial condition as suggested by Peregrine (2003). That also suggests that similarity solutions might exist.

The pressure profiles and the corresponding free surface profiles are shown in Figs. 23 and 24. In particular we select in Fig. 24 some instants like those at which the pressure and the acceleration reach their maximum. The results confirm the already observed chronology and the fact that the maximum of pressure occurs as the jet is already well developed. In addition we compare the distribution of first two components of pressure in the Bernoulli equation

$$p = -\rho\phi_{,t} - \tfrac{1}{2}\rho(\nabla\phi)^2 - \rho g y. \tag{41}$$

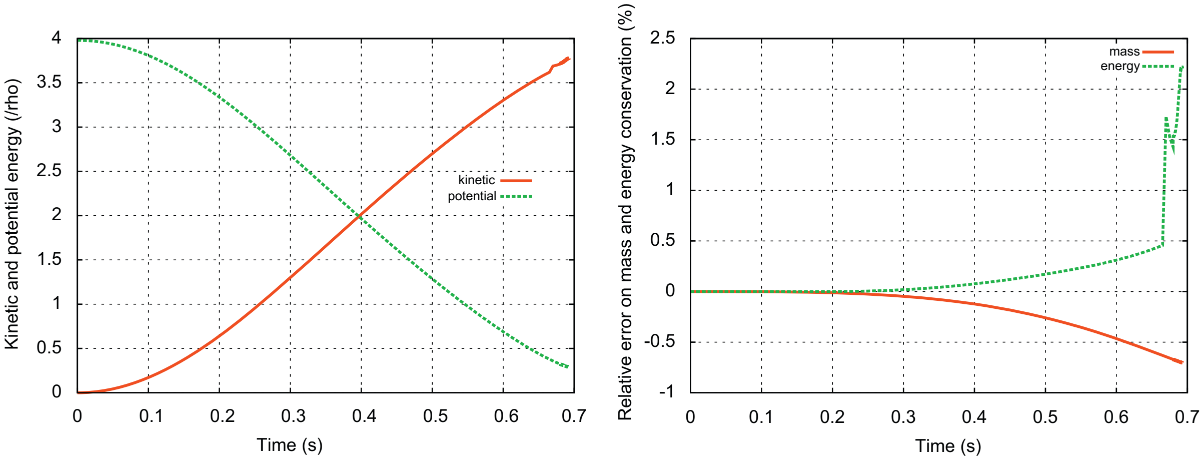

Fig. 20. Time variations of the energy components: kinetic and potential (*left*). Time variations of the relative errors on the total energy and mass conservation (*right*). The initial condition is defined in the caption of Fig. 19.

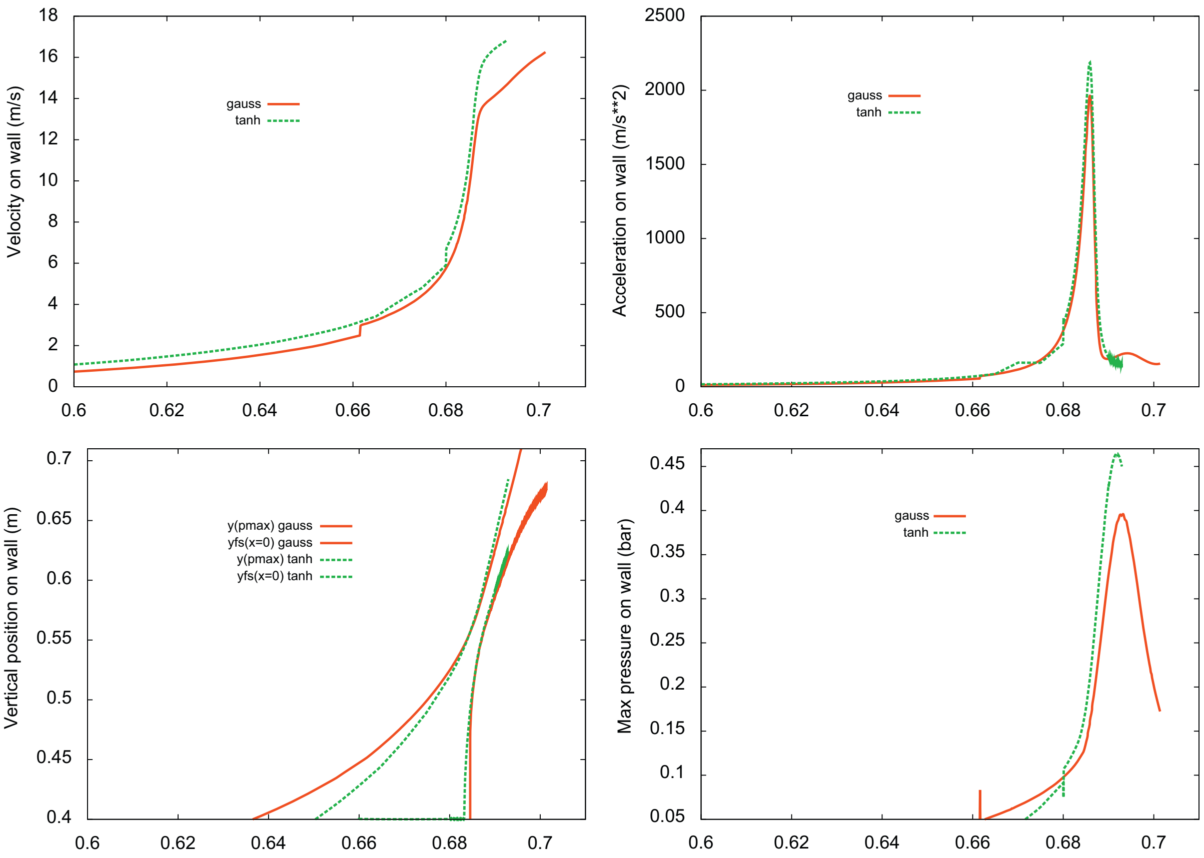

Fig. 21. Time variations of kinematics quantities. (*top left*): velocity of the intersection point (denoted $y_{x=0}$) between the free surface and the left vertical wall, (*top right*): acceleration of this point, (*bottom left*): two points $y_{x=0}$ and the vertical position of the maximum pressure (denoted $y_{p_{\max}}$), (*bottom right*): pressure peak. (tanh) refers to initial conditions defined by Eq. (24) and parameters $A=0.52$ m, $h=0.75$ m, $R=2$ and $L=4$ m. (gauss) refers to initial conditions defined by Eq. (25) and parameters $A=1$ m, $h=0.16$ m, $R=0.5$ and $L=4$ m.

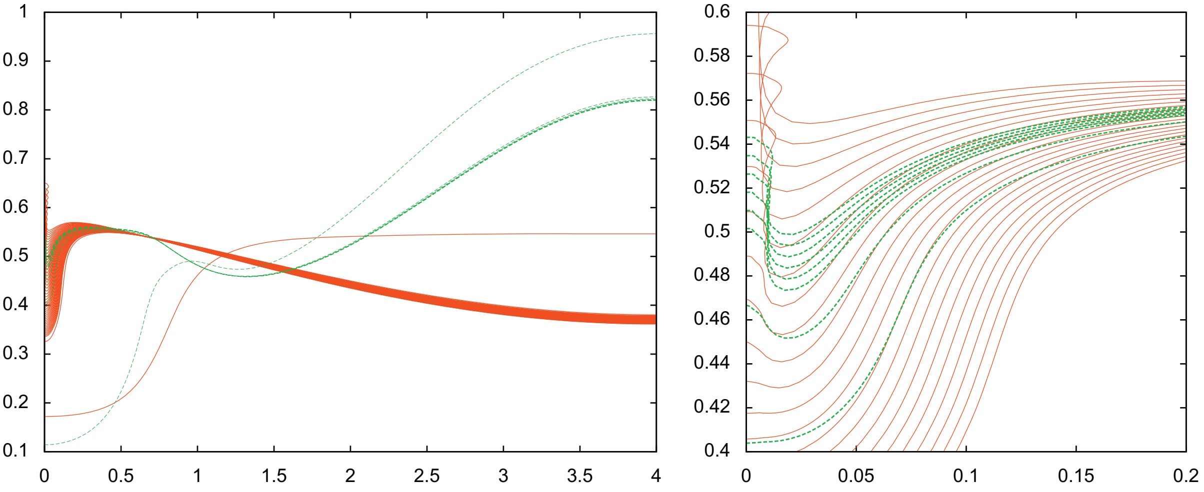

Fig. 22. Free surface profiles at different instants of two simulations starting either from initial shape of type (24) or of (25). A shift of 0.14 m is imposed to roughly adjust the points at which the free surface flips.

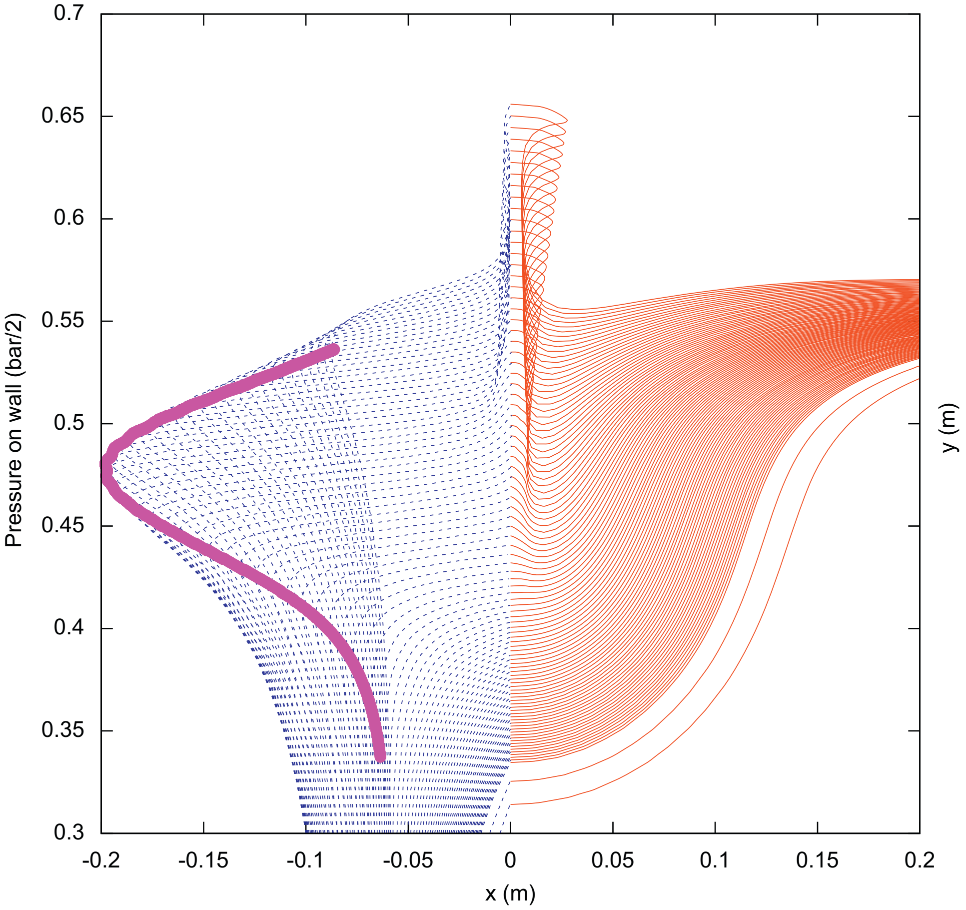

Fig. 23. See Fig. 17 for explanation. The pressure in bar in divided by 2. The initial condition is defined by Eq. (25) and parameters $A = 1\,\mathrm{m}$, $h = 0.16\,\mathrm{m}$, $R = 0.5$ and $L = 4\,\mathrm{m}$.

They have the same order of magnitude but they are opposite in sign. In the present case they are about three times or so the maximum total pressure. These spatial variations also show that fluid acceleration starts deep since the component $-\rho\phi_{,t}$ has a greater spatial interval of variation than $\frac{1}{2}\rho(\nabla\phi)^2$. We hence can expect that a bathymetry will have some influence on the initiation of the flip-through by inhibiting the run-up along the wall. In fact that is observed in Section 3.5.

3.4. *Artificial flip-through*

We perform an exercise in order (i) to examine how the flip-through depends on the remaining part of the flow and hence (ii) to reduce the number of markers. We thus use an artifact by truncating the fluid domain as soon as the parabolic shape is obtained. Fig. 25 shows an example of domain truncation. In this example the distribution of free surface elevation and the corresponding velocity potential on the left side of the cut are used to restart the code. It should be noted that the origin for the hydrostatic pressure remains obviously unchanged after truncation. The new length of the tank is now $L \approx 1.4\,\mathrm{m}$ instead of $L \approx 4\,\mathrm{m}$. We hence restart a simulation with a plausible solution of the boundary value problem since the cut becomes the new right vertical wall where a no flux condition is prescribed. As an example along the axis $x = 1.4\,\mathrm{m}$, the computed velocity before truncation is mainly horizontal and its intensity is roughly $U = 1.9\,\mathrm{m/s}$; which is very small compared to the maximum velocity reached while the flip-through is developing.

That is an artifact but it works well since preliminary numerical experiments show that this truncation does not affect either the time variation of maximum peak pressure or the fluid dynamics along the right vertical wall. However, the

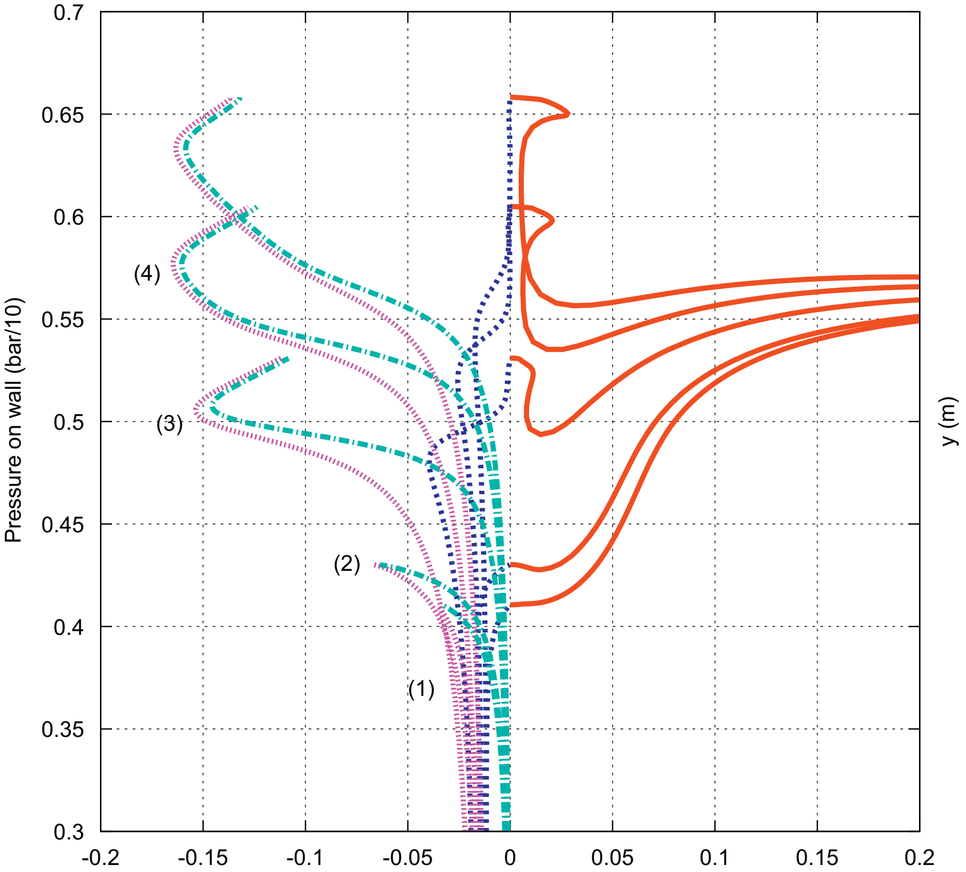

Fig. 24. Selected distribution of pressure on the left vertical wall (*left*) and corresponding free surface profile (*right*). (1) $t = 0.976929$ s: before flip-through, (2) $t = 0.978994$ s: time at which acceleration is maximum, (3) $t = 0.986298$ s: time at which pressure peak reaches its maximum, (4) $t = 0.991156$ and 0.994494 s two following instants including the last computed instant. For each instant, the vertical variation of the corresponding components of the pressure $-\rho\phi_{,t}$, and $\frac{1}{2}\rho(\nabla\phi)^2$ are plotted as well. The initial condition is defined in the caption of Fig. 23.

influence of the numerical parameters (position of the cut and possible re-gridding, *etc.*) would need to be investigated more systematically if one aimed to justify rigorously the present heuristic choice.

The locations of the sources remain unchanged after the truncation. That means that the first part of the simulation yielded enough concentration of markers in the vicinity of the smallest curvature radii, hence new markers are not introduced. For the present case we end up with 60 markers after truncation. The obtained free surface profile is plotted in Fig. 26. The source line is also plotted and it is defined according to formula (40). Fig. 27 show the time variations of the velocity of the intersection point $y_{x=0}$ between the free surface and the left vertical wall and its second time derivative, thus the acceleration of this point. These variations are quite similar to those described by Longuet-Higgins and Oguz (2005, 2007). However, there are no reasons to think that this flow contains a singularity occurring at a finite time. These results compare better with the theoretical results obtained by Cooker (2010) (see his Fig. 1). It is worth comparing the location of the instantaneous peak pressure (noted $y_{p_{\max}}$) relative to the tip of the jet. This is plotted in Fig. 27 as well. The peak pressure is thus identified at each instant and plotted in Fig. 27. Some spurious oscillations occur and they are connected to the flip of the markers at the lowest point where the curvature radius is the smallest as illustrated in Fig. 28. Increasing the number of markers does not improve the numerical solution; that is rather the contrary. The peak of acceleration may reach a very high value (here $\gamma_{\max} \approx 1800$ times the acceleration of gravity). That is of the same order of magnitude as those recorded in Peregrine (2003) or in Lugni et al. (2006). It should be noted that the duration over which the acceleration is above $2000\,\mathrm{m/s^2}$ is about $\delta t \approx 2$ ms. That gives necessary information on the requirements in terms of sampling frequency and the size of pixel, in order to capture such rapid variations by using a fast camera and image processing. We note again that the peak of acceleration precedes the maximum of

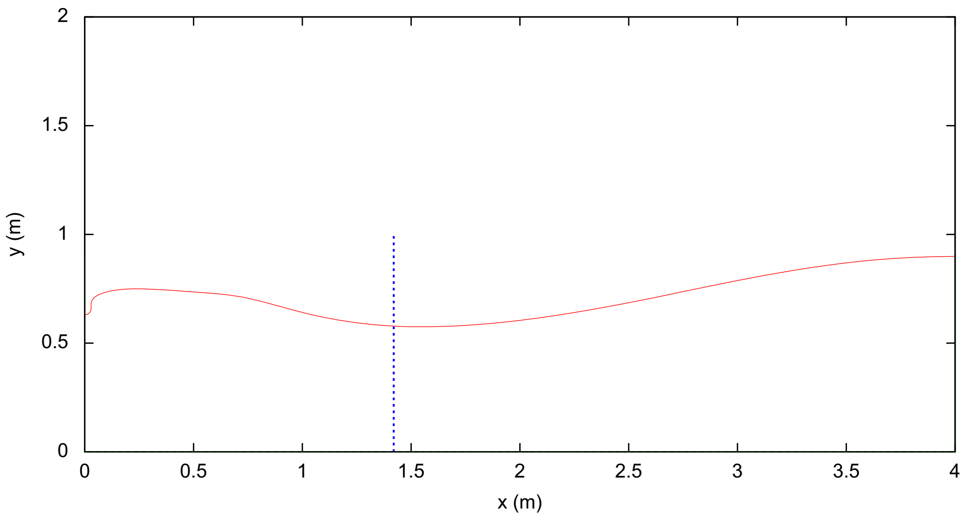

Fig. 25. Truncation of the fluid domain defined by the vertical dashed line. The distribution of free surface elevation and the corresponding velocity potential on the left side of the cut are used to restart the code.

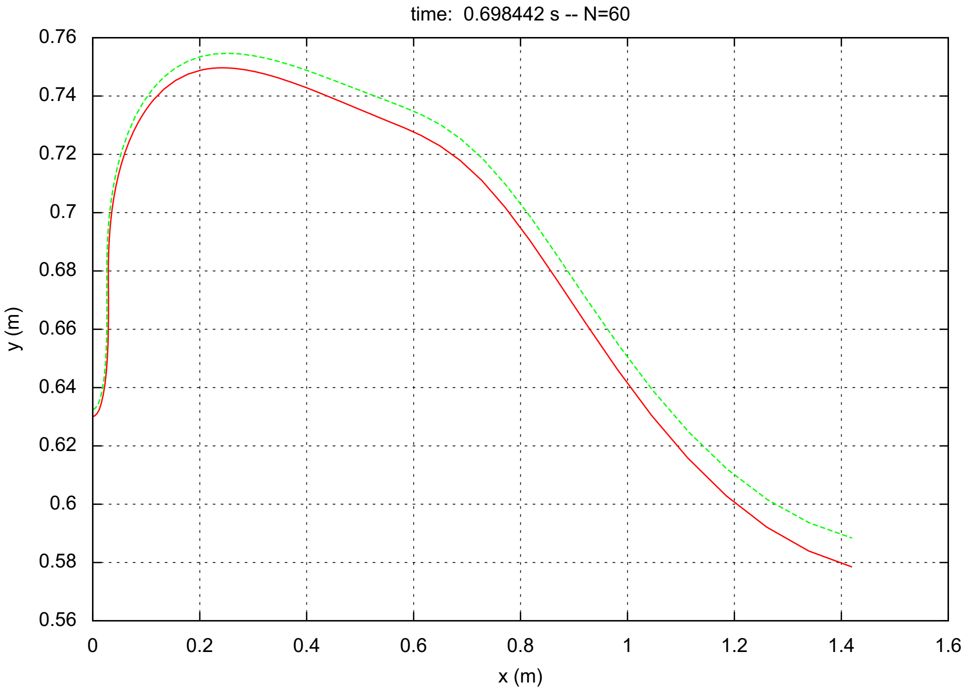

Fig. 26. Rediscretized wave profile with no additional markers but adapted distribution of sources according to formula (40). The corresponding source line is drawn.

pressure reached during the simulation; here about $p_{\max} \approx 1.3\,\mathrm{bar}$. The time interval between these two instants is $\delta t \approx 1.26\,\mathrm{ms}$, roughly one third of the duration of the present simulation. The horizontal force is computed and its maximum value made non-dimensional with $\rho g y^2_{x=0}$ is about 5. That is smaller than the maximum force computed by Bredmose et al. (2009). Some characteristic instants are selected and the corresponding free surface profiles and pressure distributions are plotted in Fig. 29. It is worth recalling that the initial instant of the simulation corresponds to the configuration sketched in Fig. 26. We hence start with an already formed parabolic shape. Four instants are examined:

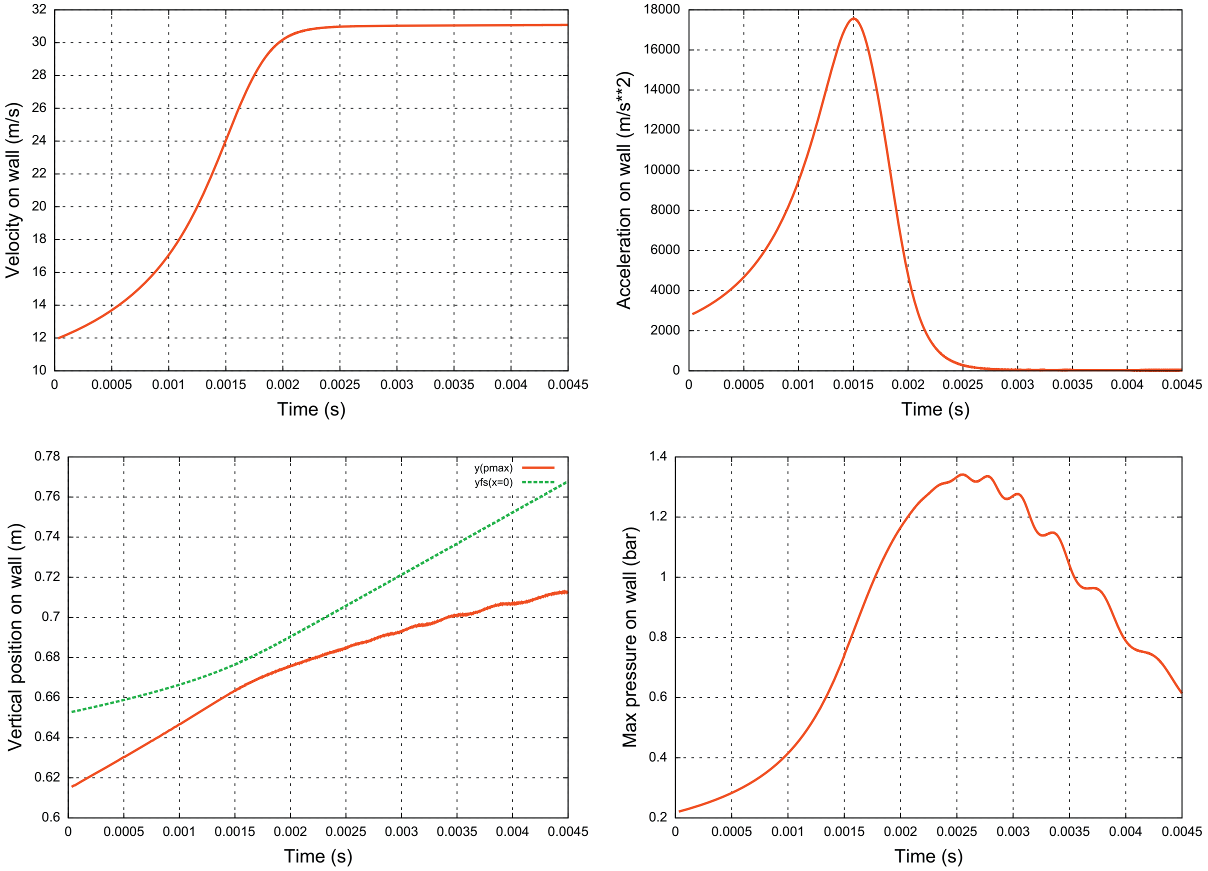

Fig. 27. See Fig. 21 for explanation. The initial condition is defined by the state of flow at time $t = 0.703874$ s starting from a first simulation with initial deformation defined by Eq. (24) with parameters $A = 0.49$ m, $h = 0.75$ m, $R = 2.4$ and $L = 4$ m. The profile is truncated at $L = 1.43$ m.

at $t = 0.000820$ s the flip-through did not occur, yet $t = 0.001506$ s is the instant at which acceleration is maximum, the pressure reaches its maximum at instant $t = 0.002772$, and 0.004550 s corresponds to the last computed time. The maximum of acceleration occurs when the free surface changes curvature at the wall. The jet develops and the maximum of pressure follows. The contribution of the two components of the pressure are plotted, namely $-\rho\phi_{,t}$ and $-\frac{1}{2}\rho(\nabla\phi)^2$; their corresponding contributions to the pressure are always opposite in sign. Their amplitude increases in time up to the instant at which the vertical velocity along the wall at the intersection point reaches a threshold, here at about $\phi_{,y} \approx 31$ m/s. Before that instant the inertial term contribution is preponderant and that is due to the increasing acceleration of the fluid.

3.5. *Influence of bathymetry on flip-through*

We shall not perform an exhaustive parametrical analysis of bathymetric influence on the flip through phenomenon. The space of parameters has too high dimension. That perspective will be the focus of future works. In fact, we simply start from the initial condition (25) and we superimpose an elliptical bathymetry at the bottom of the left vertical wall. The horizontal semi-axis is set to 1 m long and the vertical semi-axis is variable; it varies within the range $B \in [0\,\mathrm{m}, 0.1\,\mathrm{m}]$. Fig. 30 sums up the successive free surface profiles at similar instants; four instants are plotted. It should be noted that, regardless the value of B, the profiles seem to intersect at the same spatial locations. For the ten computed thicknesses B, Fig. 31 shows a snapshot of the free surface profiles at the same instant $t = 0.97956$ s whatever the thickness of the bathymetry. A zoom is plotted in the same figure. As expected, we observe that the only part of the flow which is significantly affected, is above the changing bathymetry. Elsewhere the influence is hardly noticeable. In Fig. 31, the zoom view shows: the flatter the bathymetry profile, the earlier the flip-through; the thicker the bathymetry

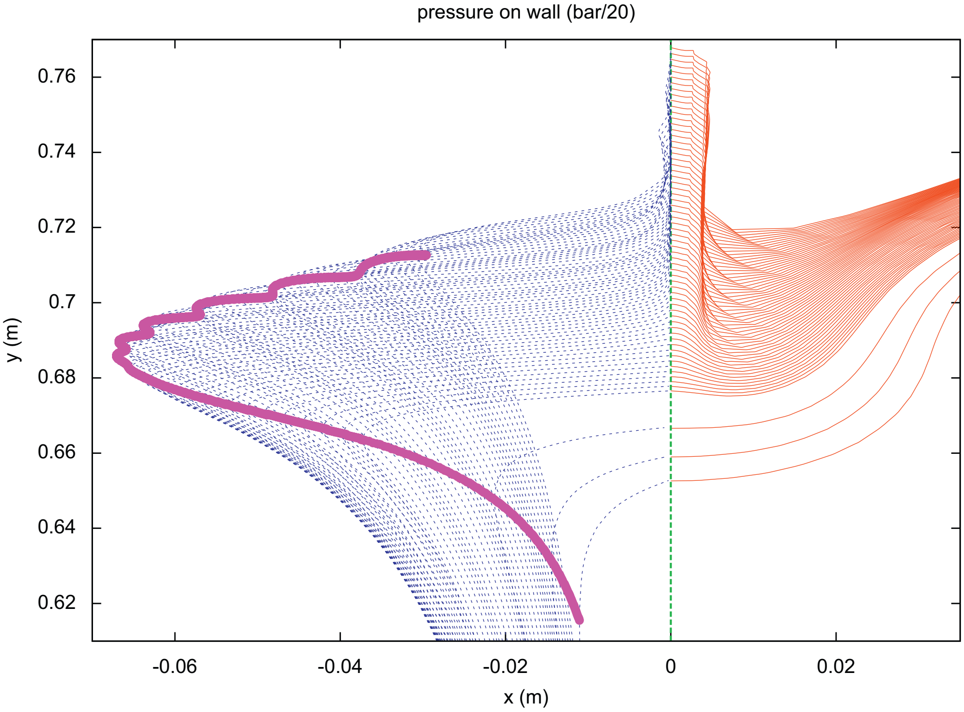

Fig. 28. See Fig. 17 for explanation. The pressure in bar in divided by 20. The initial condition is defined in the caption of Fig. 27.

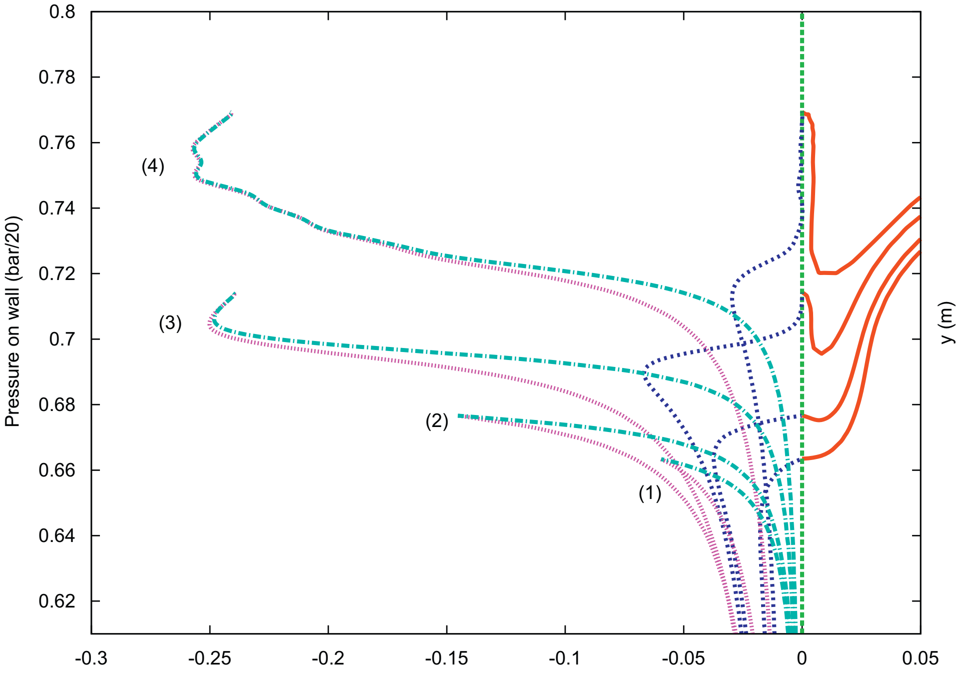

Fig. 29. Selected distribution of pressure on the left vertical wall (*left*) and corresponding free surface profile (*right*). (1) $t = 0.000820$ s: before flip-through, (2) $t = 0.001506$ s: time at which acceleration is maximum, (3) $t = 0.002772$ s: time at which pressure peak reaches its maximum, (4) $t = 0.004550$ s: last computed time. For each instant, the vertical variation of the corresponding components of the pressure $-\rho\phi_{,t}$, and $\frac{1}{2}\rho(\nabla\phi)^2$ are plotted as well. The initial condition is defined in the caption of Fig. 27.

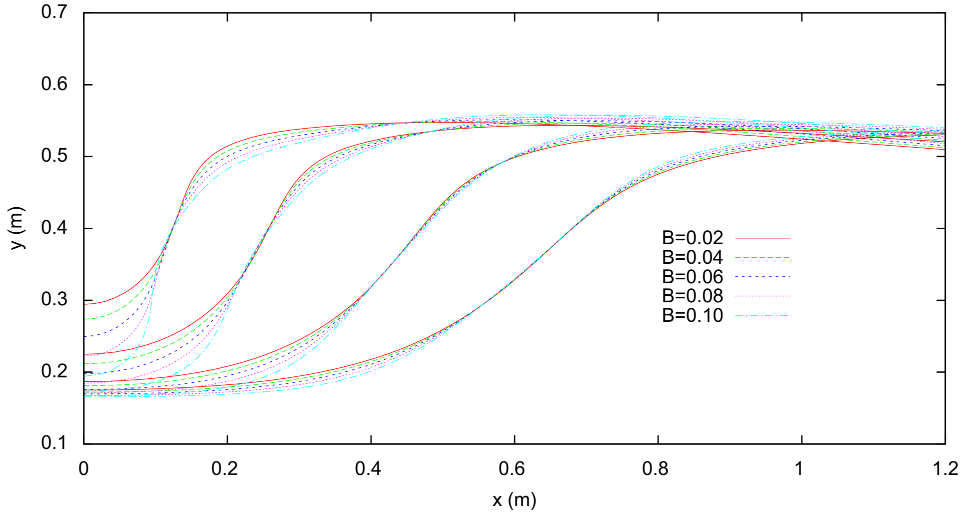

Fig. 30. Free surface profiles at four similar instants $t = 0.770739$, 0.841449, 0.912159, 0.954868 s for a varying thickness of the elliptical bathymetry $B \in [0.02\,\text{m} : 0.1\,\text{m}]$. The initial condition is defined by Eq. (25) and parameters $A = 1$ m, $h = 0.16$ m, $R = 0.5$ and $L = 4$ m.

profile, the more vertical the front of the arriving wave. In Fig. 32, we can compare the kinematics at the vertical wall. The time variations of $y_{x=0}$ and its first and second time derivatives are plotted. The general behavior is standard, the acceleration reaches a maximum and then the velocity varies more slowly, but here the velocity never reaches a threshold. In the present case, for $B < 0.04$ m, the run-up goes on for a long duration until a small overturning crest appears, roughly above $t = 0.98$ s. We are mainly interested in what occurs before that instant. More precisely we identify the time at which the maximum acceleration is reached. Fig. 33 show the variation of the maximum of acceleration reached at the intersection point $y_{x=0}$, in terms of the bathymetry thickness B. The variation of the instant at which the maximum acceleration is reached at the intersection point $y_{x=0}$ is plotted as well. The two curves are not monotonical. We can conclude that two different scenarios are likely to occur. In Fig. 32 the interval of time variation of the acceleration is shortened so that we can plot arrows corresponding to increasing thickness. There are two arrows hence illustrating the non-monotonical behavior. The transition between the two scenarios seems to occur at $B \approx 0.05$ m. Below, it is questionable whether or not we are witnessing an actual flip-through. Above $B \approx 0.05$ m, we observe a clear vertical front and a nascent vertical jet. We do not perform any computation of the pressure since this requires a great deal of computational time; that is due to the use of conformal mappings. However, we can expect that the maxima of pressure become higher and higher above $B \approx 0.05$ m.

4. Conclusion

The nonlinear free-surface problem in potential theory is solved by using a desingularized technique combined with conformal mappings. This combination of techniques allows us (a) to reduce the number of unknowns, thus the rank of the linear systems to solve, and (b) to provide a reasonably good stability of time simulation.

Some numerical aspects of the problem are investigated here. In particular the analysis of mass and energy conservation laws shows on the one hand the importance of an arbitrary additive constant to the velocity potential and on the other hand the influence of the desingularizing distance. Recommendations are listed regarding their choice for the present applications. This can be considered as a drawback of the present method; however, the most suitable choice leads to stable computations thus avoiding artificial techniques such as re-gridding or smoothing which are necessary when using a standard BEM approach.

Rapid and robust algorithms are necessary to study the flip-through phenomenon. The results obtained are in good agreement with experimental data and other numerical results. The flip-through phenomenon is identified as a transition between standard run-up along a wall and the formation of an air pocket. High accelerations and high pressures are reached within a very short time period. This kind of flow is shown to be very sensitive to the variation of parameters but it does not depend much on the type of wave which yields it. For two types of initial conditions, it is

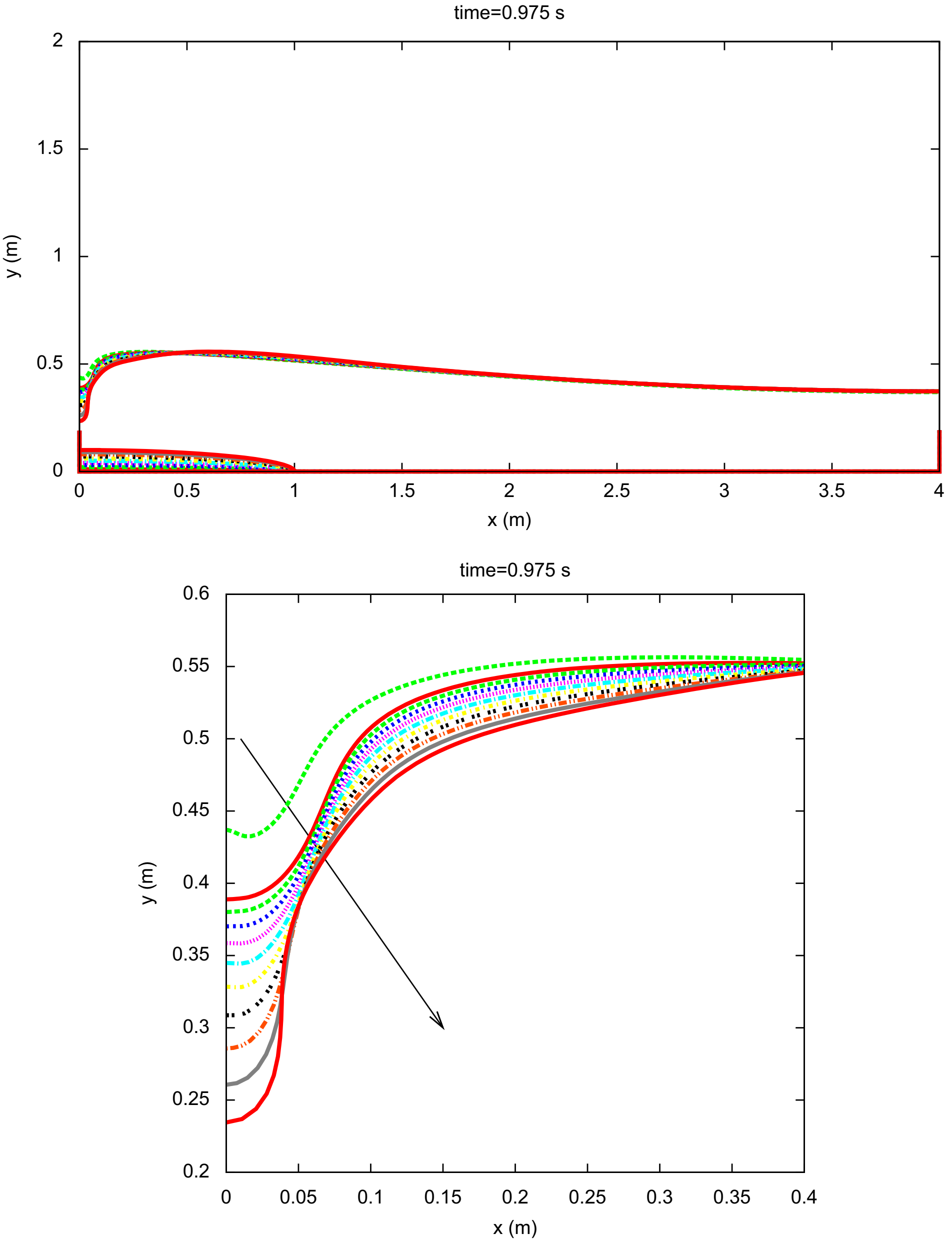

Fig. 31. Free surface profiles at the same instant $t = 0.975$ s for a varying thickness of the elliptical bathymetry. The initial condition is defined in the caption of Fig. 30. The arrow shows the increasing thickness of the elliptical bathymetry B.

observed that the peak of acceleration precedes the peak of pressure distribution along the vertical wall, as flip-through develops. For the application cases considered here, we may conclude that the maximum of pressure always occurs at the root of the jet. It is also observed that bathymetry plays an important role by influencing the run-up along the wall.

This study points the way to at least two new directions of research. Firstly comparisons with experimental data are strongly required since very high loads are computed as the vertical jet develops along the wall. The existing experimental studies have already shown the difficulties encountered due the very short duration of the phenomenon. As it is known that flip-through does not depend much on the type of initial conditions, there are alternative ways to capture it while repeatability is better controlled. One way is to start from a soliton riding on a sloping beach; its

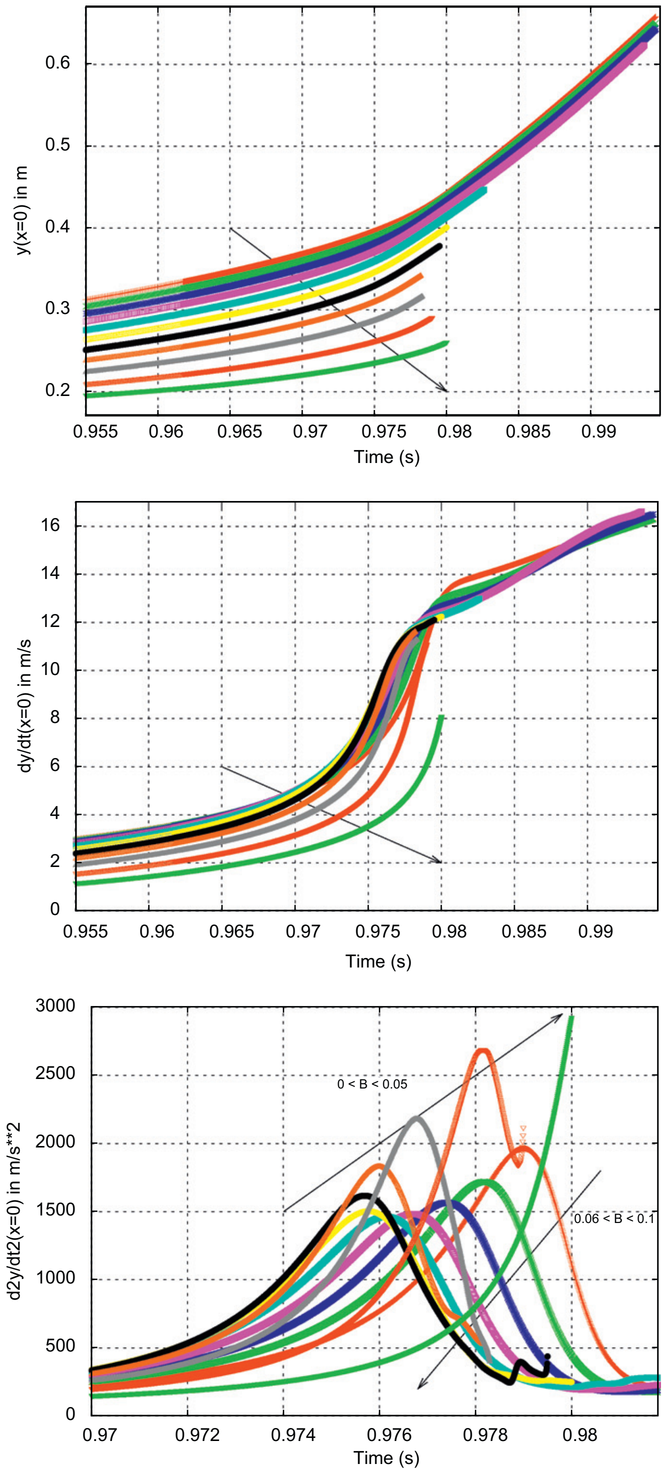

Fig. 32. Time variations of (*top*) vertical position of the intersection point $y_{x=0}$ between the free surface and the left vertical wall, (*middle*) its velocity, (*bottom*) its acceleration. Arrows show the increasing thickness of the elliptical bathymetry B.

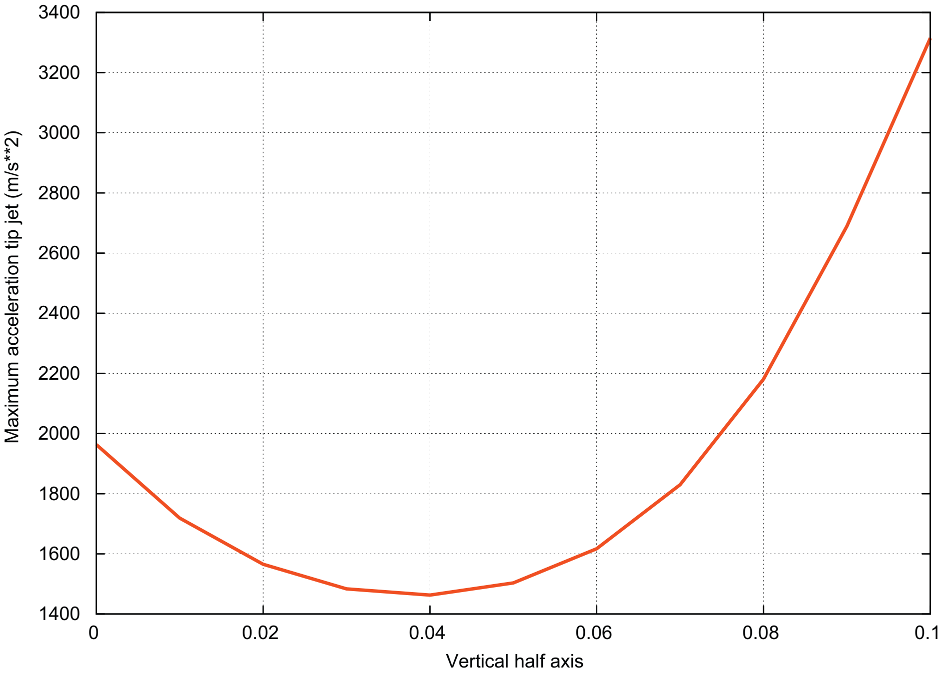

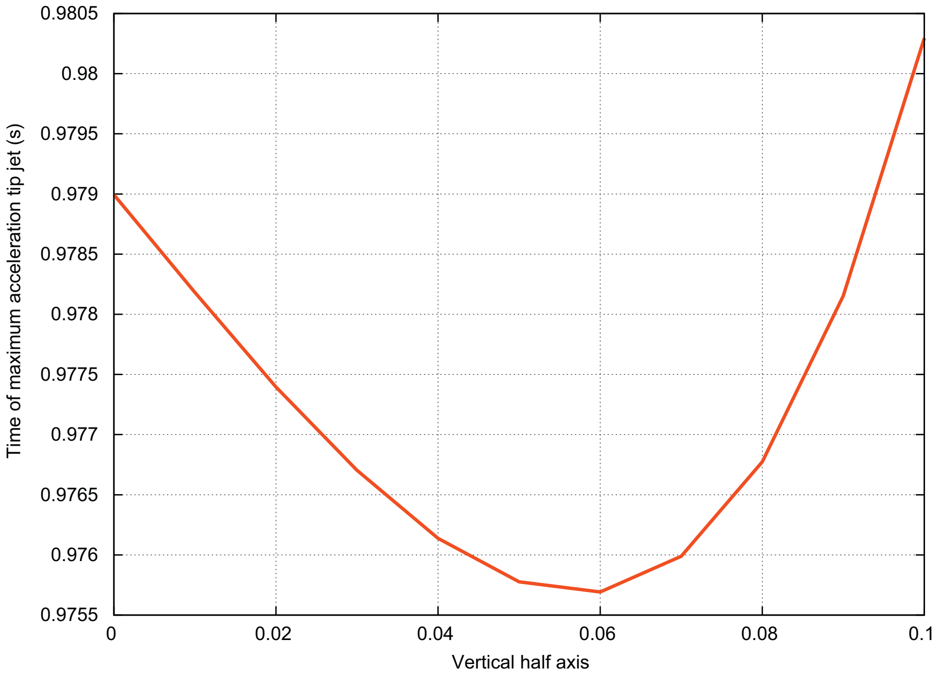

Fig. 33. (*top*): Variation of the maximum of acceleration reached at the intersection point $y_{x=0}$, in terms of the bathymetry thickness B. (*bottom*): Variation of the instant at which the maximum of acceleration is reached at the intersection point $y_{x=0}$, in terms of the bathymetry thickness B.

generation with a wavemaker is much simpler than a focused wave. Thus the influence of local bathymetry on the jet's development would be better investigated. As a consequence, not only the two-dimensionality of the flow is better assessed, but also the statistical properties of pressure or the measurement of the local curvature radius at the wall are better controlled.

The second direction of research is mathematical. It is worth while noting the influence of an arbitrary additive constant to the velocity potential on the conservation laws. That means the matrix conditioning must be better investigated. However, the corresponding mathematical problem becomes very tricky since the free surface is highly distorted.

Acknowledgements

This work is carried out in SLOSHEL project whose overview has been presented at the 19th ISOPE conference held in Osaka (Japan) 2009. The author would like to acknowledge funding from Bureau Veritas.

References

Alves, C.J.S., 2009. On the choice of source points in the method of fundamental solutions. Engineering Analysis with Boundary Elements 33, 1348–1361.

Bogomolny, A., 1985. Fundamental solutions method for elliptic boundary value problems. SIAM Journal on Numerical Analysis 22, 644–669.

Bredmose, H., Hunt-Rabi, A., Jayaratne, R., Bullock, G.N., 2010. The ideal flip-through impact: experimental and numerical investigation, Journal of Engineering Mathematics, 67(1–2), 115–136.

Bredmose, H., Peregrine, D.H., Bullock, G.N., 2009. Violent breaking wave impacts. Part 2: modelling the effect of air. Journal of Fluid Mechanics, 641, 389–430.

Cao, Y., Schultz, W.W., Beck, R.F., 1991. A three-dimensional desingularized boundary integral method for potential problems. International Journal Numerical Method in Fluids 11, 785–803.

Chambarel, J., Kharif, C., Kimmoun, O., 2010. Generation of two-dimensional steep water waves on finite depth with and without wind. European Journal of Mechanics/B Fluids, 29(2), 132–142.

Christiansen, S., 1976. On Kupradze's functional equations for plane harmonic problems. In: Gilbert, R.P., Weinacht, R.J. (Eds.), Function Theoretic Methods in Differential Equations. Pitman, London, pp. 205–243.

Cooker, M.J., Peregrine, D.H., 1990. A model of breaking wave impact pressures. In: Proceedings of 22nd ASCE Conference Coastal Engineering, Holland, pp. 1473–1486.

Cooker, M.J., 2010. The flip-through of a plane inviscid jet with a free surface. Journal of Engineering Mathematics, 67(1–2), 1–9.

Faltinsen, O.M., Rognebakke, O.F., Lukovski, I.A., Timokha, A.N., 2000. Multidimensional modal analysis of nonlinear sloshing in a rectangular tank with finite water depth. Journal of Fluid Mechanics 407, 201–234.

Faltinsen, O.M., Timokha, A.N., 2009. Sloshing. Cambridge University Press.

Gao, Z.L., Zou, Z.J., 2008. A three-dimensional desingularized high order panel method based on NURBS. Journal of Hydrodynamics Series B 20 (2), 137–146.

Goldberg, M.A., 1995. The method of fundamental solutions for Poisson's equation. Engineering Analysis with Boundary Elements 6, 205–213.

Halsey, N.D., 1979. Potential flow analysis of multielement airfoils using conformal mapping. AIAA Journal 17, 1281–1288.

Ives, D.C., 1976. A modern look at conformal mapping including multiply connected regions. AIAA Journal 14 (8), 1006–1011.

Kimmoun, O., Malenica, Š., Scolan, Y.-M., 2009. Fluid structure interactions occurring at a flexible vertical wall impacted by a breaking wave. In: Proceedings of the Nineteenth International Offshore and Polar Engineering Conference Osaka, Japan, pp. 308–315.

Kupradze, V.D., Aleksidze, M.A., 1963. An approximate method of solving certain boundary-value problems. Soobshcheniya Akademii Nauk Gruzinskoi SSR 30, 529–536 (in Russian).

Krasny, R., 1986. Desingularization of periodic vortex sheet roll-up. Journal of Computational Physics 65, 292–313.

Lalli, F., 1997. On the accuracy of the desingularized boundary integral method in free surface flow problems. International Journal for Numerical Methods in Fluids 25 (10), 1163–1184.

Longuet-Higgins, M.S., Oguz, H., 2005. Critical microjets in collapsing cavities. Journal of Fluid Mechanics 290, 183–201.

Longuet-Higgins, M.S., Oguz, H., 2007. Critical microjets in surface waves and collapsing cavities. Philosophical Transactions of the Royal Society of London A 355, 625–639.

Longuet-Higgins, M.S., 2001. Vertical jets from standing waves: the bazooka effect. Philosophical Transaction of the Royal Society of London A 457, 495–510.

Lugni, C., Brocchini M., Dolcini, A., Palladino, F., Bulgarelli, U.P., Faltinsen, O.M., 2005. An experimental investigation on the flip-through phenomenon. In: Proceedings of 20th International Workshop on Water Waves and Floating Bodies, paper No. 39.

Lugni, C., Brocchini, M., Faltinsen, O.M., 2006. Wave impact loads: the role of the flip-through. Physics of Fluids 18 (12).

Mathon, R., Johnston, R.L., 1977. The approximate solution of elliptic boundary-value problems by fundamental solutions. SIAM Journal on Numerical Analysis 14 (4), 638–650.

Peregrine, D.H, 2003. Water-wave impact on walls. Annual Review of Fluid Mechanics 35, 23–43.

Pozrikidis, C., 2000. On the method of functional equations and the performance of desingularized boundary element methods. Engineering Analysis with Boundary Elements 24 (1), 3–16.

Scolan, Y.M., Kimmoun, O., Branger, H., Remy, F., 2007. Nonlinear free surface motions close to a vertical wall. Influence of a local varying bathymetry. In: Proceedings of 22nd International Workshop on Water Waves and Floating Bodies, pp. 177–180.

Scolan, Y.-M., Etienne, S., 2008. On the use of conformal mapping for the computation of hydrodynamic forces acting on bodies of arbitrary shape. Part 1: simply connected body. Journal of Engineering Mathematics 60 (2), 209–220.

Smyrlis, Y.-S., Karageorghis, A., 2001. Some aspects of the method of fundamental solutions for certain harmonic problems. Journal of Scientific Computing 16 (3), 341–371.

Spiegel, M.R., 1999. Complex variable with an introduction to conformal mapping and its applications. In: Schaum's Outlines Series 32nd Ed. McGraw-Hill 313pp.

Theodorsen, T., Garrick, I.E., 1933. General potential theory of arbitrary wing sections. NACA Report 452, 177–209.

Tuck, E.O., Solution of nonlinear free-surface problems by boundary and desingularised integral equation techniques, invited lecture, In: Noye, J., Teubner, M., Gill, A. (Eds.), Computational Techniques and Applications: CTAC'97. World Scientific, Singapore, pp. 11–26.

Warchawski, S.E., 1945. On Theodorsen's method of conformal mapping of nearly circular regions. Quarterly Journal of Applied Mathematics 3 (2), 12–28.

Webster, W.C., 1975. The flow about arbitrary three-dimensional smooth bodies. Journal of Ship Research 19, 206–218.

Young, D.L., Hwang, W.S., Tsai, C.C., Lu, H.L., 2005. Accuracy of desingularized boundary integral equations for plane exterior potential problems. Engineering Analysis with Boundary Elements 29 (3), 224–231.

Zhang, X.T., Khoo, B.C., Lou, J., 2006. Wave propagation in a fully nonlinear numerical wave tank: a desingularized method. Ocean Engineering 33, 2310–2331.

Zhang, S., Yue, D.K.P., Tanizawa, K., 1996. Simulation of plunging wave impact on a vertical wall. Journal of Fluid Mechanics 327, 221–254.